Single-Cell Epigenomics Uncovers Heterochromatin Instability and Transcription Factor Dysfunction during Mouse Brain Aging

Maria Luisa Amaral[1,2], Sainath Mamde[1], Michael Miller[3], Xiaomeng Hou[3], Jessica Arzavala[4], Julia Osteen[4], Nicholas D. Johnson[4], Elizabeth Walker Smoot[3], Qian Yang[3], Emily Eisner[3], Qiurui Zeng[5,6], Cindy Tatiana Báez-Becerra[4], Jacqueline Olness[3], Joseph Colin Kern[3], Jonathan Rink[4], Ariana Barcoma[4], Silvia Cho[4], Stella Cao[4], Nora Emerson[4], Jasper Lee[4], Jackson Willier[4], Timothy Loe[1], Henry Jiao[3], Songpeng Zu[1], Quan Zhu[3], Sebastian Preissl[3], Allen Wang[3], Joseph R. Ecker[5,8], Maria Margarita Behrens[4]*, Bing Ren[1,3,7]*

1. Department of Cellular and Molecular Medicine, University of California, San Diego School of Medicine, La Jolla, CA, USA
2. Bioinformatics and Systems Biology Program, University of California, San Diego, La Jolla, CA, USA
3. Center for Epigenomics, University of California, San Diego, School of Medicine, La Jolla, CA, USA
4. Computational Neurobiology Laboratory, The Salk Institute for Biological Studies, La Jolla, CA, USA
5. Genomic Analysis Laboratory, The Salk Institute for Biological Studies, La Jolla, CA, USA
6. Division of Biological Sciences, University of California, San Diego, La Jolla, CA, USA
7. Institute of Genomic Medicine, Moores Cancer Center, School of Medicine, University of California San Diego, La Jolla, CA, USA
8. Howard Hughes Medical Institute, The Salk Institute for Biological Studies, La Jolla, CA, USA

*Correspondence: biren@health.ucsd.edu (B.R.), mbehrens@salk.edu (M.M.B.)

Highlights

- Single-cell multimodal profiling across eight brain regions reveals coordinated chromatin and transcriptional shifts during aging
- Age-related depletion of progenitor cells coincides with dysregulation of key lineage specific transcription factors
- Cell identity maintenance is compromised with the decline of master transcription factors
- Heterochromatin destabilization accompanied by activation of AP-1, transposable elements, pseudogene families, and long non-coding RNAs

Summary

The mechanisms regulating transcriptional changes in brain aging remain poorly understood. Here, we use single-cell epigenomics to profile chromatin accessibility and gene expression across eight brain regions in the mouse brain at 2, 9, and 18 months of age. In addition to a significant decline in progenitor cell populations, we observed widespread and concordant changes of transcription and chromatin accessibility during aging in glial and neuronal cell types. These alterations are accompanied by dysregulation of master transcription factors and a shift toward stress-responsive programs, indicating a progressive loss of cell identity with aging. We also identify region- and cell-type-specific heterochromatin decay, characterized by increased accessibility at H3K9me3-marked domains, activation of transposable elements, and upregulation of long non-coding RNAs, particularly in glutamatergic neurons. Together, these results reveal age-related disruption of heterochromatin maintenance and transcriptional programs, identify vulnerable brain regions and cell types, and pinpoint key molecular pathways altered in brain aging.

Introduction

Aging is accompanied by widespread cellular and molecular changes in the brain, which contribute to cognitive decline, reduced neural plasticity, and increased vulnerability to neurodegenerative diseases[1]. Detailed characterization of these changes holds the key to a better understanding of the mechanisms of organismal aging. While gene expression alterations have been extensively analyzed at single-cell resolution[2,3], the transcriptional regulatory mechanisms shaping these changes remain largely unresolved. Epigenetic processes, manifested as chromatin accessibility, DNA methylation, histone modifications, and 3D chromatin organization, play a crucial role in defining cellular identity and responsiveness to environmental cues[4], yet how epigenomic landscapes shift with age across different brain regions and cell types is not well understood. Here, we present a comprehensive analysis of cell-type- and brain-region-resolved chromatin accessibility of brain aging, integrating single-cell Assay for Transposase Accessible Chromatin using sequencing (ATAC-seq) and RNA-seq data

across eight mouse brain regions. By resolving epigenomic changes at single-cell resolution, we uncover regulatory mechanisms that contribute to aging-associated transcriptional shifts and cellular dysfunction.

Previous studies have uncovered common hallmarks of aging—including genomic instability, stem cell exhaustion, mitochondrial dysfunction, and inflammation—shared across tissues and model organisms[5]. More recently, epigenetic alterations such as chromatin accessibility dynamics, DNA methylation changes, and histone modifications have been proposed as key regulators of aging[6], contributing to a progressive loss of transcriptional and regulatory fidelity that affects cellular identity and function[7]. Notably, epigenetic aging is also a reversible process, as ectopic expression of pluripotency factors[8], activation of SIRT6 histone deacetylase[9,10], and modulation of other histone-modifying enzymes[11,12] have been shown to mitigate certain aging phenotypes. However, prior studies on brain aging largely rely on bulk tissue analyses, which obscure cell-intrinsic aging effects and fail to capture regulatory changes across different brain cell types and regions. Given the brain's cellular diversity, a cell-type-resolved analysis of chromatin aging is essential to distinguish intrinsic regulatory changes from shifts in cellular composition, especially since neurodegenerative diseases disproportionately affect specific brain regions and cell populations—such as dopaminergic neurons in the substantia nigra in Parkinson's disease[13], oligodendrocytes in the white matter in multiple sclerosis[14], and hippocampal neurons in Alzheimer's disease[15]. A deeper understanding of how chromatin landscapes change during aging at the cell-type level will provide insights into how regulatory changes contribute to neurodegeneration and could uncover new therapeutic opportunities.

Previous studies have characterized transcriptomic changes in aging at the single-cell level, including large-scale efforts such as Tabula Muris Senis[2], which cataloged aging signatures across multiple tissues, and a recent brain-wide atlas of aging[3], which profiled 1.2 million neuronal and glial transcriptomes across the mouse brain. In addition to scRNA-seq, spatial transcriptomics has revealed white matter as particularly affected by aging[16]. These studies revealed that different cell types and spatial locations exhibit distinct transcriptional aging signatures. While transcriptomic atlases provide valuable insights, they alone do not capture the regulatory mechanisms driving transcriptional shifts.

The epigenome is essential for maintaining cell identity and gene regulation, yet how the epigenome changes with aging across different brain cell types and regions remains poorly understood. Focusing on chromatin accessibility, our previous study revealed that excitatory neurons in the mouse frontal cortex lose H3K9me3-marked heterochromatin with age, leading to increased accessibility at transposable elements and normally repressed genomic regions[17]. These findings suggest that heterochromatin instability may be a key feature of neuronal aging. However, a comprehensive, multi-region, single-cell chromatin accessibility map of the aging brain has been lacking. Here, we address this gap by profiling chromatin accessibility in over 1.1 million cells across eight brain regions in both male and female mice. Additionally, our companion paper investigates age-associated DNA methylation changes and alterations in 3D genome organization.

Briefly, we report here a single-cell, multi-region chromatin accessibility and transcriptomic atlas of brain aging, generated through profiling of eight brain regions in male and female mice at 2, 9, and 18 months of age. Using a combination of single-cell assays including snATAC-seq, 10X multiome (single nucleus combined ATAC-seq and RNA-seq), and spatial transcriptomics, we examined the Prefrontal Cortex (FC), Anterior Hippocampus (AHC), Posterior Hippocampus (PHC), Entorhinal Cortex (EC), Nucleus Accumbens (NAC), Caudate Putamen (CP), Amygdala (AMY), and Periaqueductal Gray (PAG/PCG, RLP) (Table S1). These regions were selected due to their critical roles in cognition, memory, and emotional regulation, as well as their known vulnerabilities to age-related decline and neurodegenerative processes[18]. Integrative analysis showed a dramatic age-associated decline of three progenitor populations, accompanied by age-associated chromatin remodeling and transcriptional shifts. Major neuronal and glial populations display broad transcription factor dysregulation, chromatin accessibility changes, and disruptions in regulatory landscapes that drive shifts in cellular function. Finally, we observe widespread aging-associated chromatin changes, including heterochromatin destabilization, transposable element reactivation, and increased accessibility at stress-responsive elements, which emerge as defining features of brain aging. Together, this work provides insights into the transcriptional regulatory mechanisms underlying neuronal and glial aging in the mouse brain.

Results

Single-Nucleus Multi-Omics Analysis of the Aging Mouse Brains

To determine how chromatin accessibility and transcriptional programs shift during aging, we profiled eight brain regions across three ages (2, 9, and 18 months) in adult mice using single-nucleus ATAC-seq (snATAC-seq), single-nucleus Multiome (ATAC-seq + RNA-seq), and MERFISH spatial transcriptomics (Table S1). For snATAC-seq, we profiled each brain region in 2 biological replicates, each containing pooled brain tissues dissected from 3-7 mice, of 9-month-old and 18-month-old males, while incorporating our previously generated 2-month-old male data[19]. For female samples, we generated single-nucleus 10X multiome data, extending our analysis to both modalities (ATAC-seq and RNA-seq) from all three age groups. In total, we analyzed chromatin accessibility in 1,116,638 cells, RNA expression in 368,491 cells, and spatial transcriptomics in 500,353 cells, obtaining a comprehensive view of age-dependent gene regulation and cellular composition (Figure 1a,b). We processed snATAC-seq data using SnapATAC2 and scRNA-seq + MERFISH data using Seurat[20]. Glial populations were broadly distributed across regions, while neuronal populations showed brain region specificity, consistent with region-specific neuronal specialization (Figure S1c). Batch correction with Harmony[21] minimized technical effects between the male snATAC-seq and female 10x Multiome datasets, revealing no major batch effects (Figure S1b). Genome browser tracks of the age-associated gene C4b[22] illustrate its consistent upregulation across brain regions, modalities, and sexes, demonstrating our ability to capture age-associated molecular changes (Figure S8a). More broadly, these changes in gene expression and chromatin accessibility are reflected as subtle gradients within cell clusters (Figure S1d-f). Among 80 distinct cell types identified using marker genes and integration with a single-cell transcriptomic atlas of the adult mouse brain[23], the most abundant populations were oligodendrocytes, dentate gyrus (DG)

glutamatergic neurons, and striatal D12 medium spiny neurons (Figure S1g). Notably, three progenitor cell populations showed significant age-related declines in cell abundance: Immature oligodendrocytes (IOL), OB-STR-CTX inhibitory immature neurons (IMN), and DG progenitors (Figure 1c,d).

To systematically characterize age-related chromatin remodeling, we identified open chromatin regions and candidate cis-regulatory elements (cCREs) in each cell type using MACS3[24] (Methods), revealing 881,231 combined cCREs across all cell types (Figure S2a), with 724,636 of these overlapping a previous atlas of chromatin accessibility in the adult mouse brain[25]. A majority of cCREs were cell type-specific (Figure S2b). We assessed differential chromatin accessibility between 2-month-old and 18-month-old samples across three levels of resolution: All cell types combined, within each cell type across brain regions, and within each cell type further stratified by region and sex. We defined significant changes using an adjusted p-value < 0.01 and fold changes (|logFC| > 0.5). This analysis revealed widespread chromatin remodeling with aging. At the most granular level, 88,555 cCREs exhibited significant increases in accessibility in at least one combination of celltype, region, and sex, with 30,994 unique to a single comparison. Conversely, 70,734 cCREs showed significant decreases, with 27,307 unique to a single combination. Some loci were recurrently altered across multiple comparisons: 492 cCREs were upregulated in ≥10 combinations of celltype, region, and sex, including a heterochromatin hotspot (chr13:68173417-68173918) previously linked to aging-related chromatin changes[17]. Strikingly, the most highly differential peaks across the genome were consistent between males and females, with several gene clusters—including the Killer cell lectin-like receptor (Klra), Secretoglobin (Scgb), Olfactory receptor (Olfr), Prostate and testis expressed (Pate), and Protocadherin gamma (Pcdhg) gene families—alongside intergenic regions, showing strong upregulation in neuronal aging (Figure S3a,b). To complement our chromatin accessibility analysis, we performed differential gene expression analysis using MAST, adjusting for brain region, mitochondrial percentage, ribosomal percentage, and replicate as latent variables[26]. This analysis revealed widespread transcriptional changes across glutamatergic, GABAergic, and non-neuronal cell types with aging (Figure S4a, S5a, S6a; Methods). Aging alters chromatin accessibility and transcriptional programs in a cell-type-specific manner. In the following sections, we explore progenitor populations that decline with age and regulatory changes within major neuronal and glial cell types.

Loss of Progenitor Populations in Aging Brains

Progenitor cells contribute to cellular renewal and plasticity during brain development. We identify three progenitor populations that experience dramatic declines in cell proportion with age. Among these, Dentate Gyrus (DG) progenitors exhibit the most striking reduction, decreasing from ~3% abundance in 2-month-old brains to <0.01% in both the anterior and posterior hippocampus (Figure 2d). These cells reside within one of the two major neurogenic niches in the adult brain—the dentate gyrus—where they give rise to excitatory granule neurons. The other principal neurogenic niche, the subventricular zone (SVZ), produces inhibitory neurons that migrate to the olfactory bulb. In line with this, we identified a second declining population—olfactory bulb immature inhibitory neuron-like cells annotated as OB-STR-

CTX Inh IMN[23]. These cells are primarily found in the nucleus accumbens, caudate putamen, and hippocampus, comprising ~4% of cells at 2 months, but declining with age at varying rates (Figure 2d). The third progenitor population showing dramatic age-related decline is an intermediate cell type between oligodendrocyte progenitor cells and mature oligodendrocytes, known as immature oligodendrocytes (IOLs). This population consistently decreases across brain regions, from ~2% to ~0.1% with aging, aligning with prior findings of impaired remyelination in the aging brain[27] (Figure 2c,d). These changes in progenitor cell proportions were observed in both the snATAC-seq and 10x Multiome datasets. Additionally, MERFISH spatial transcriptomic profiling confirmed the age-related, region-specific depletion of DG progenitors, OB-STR-CTX Inh IMN, and IOLs (Figure 2a–c). Notably, in aged brains, remaining progenitor cells were predominantly localized to canonical neurogenic niches. Because MERFISH captures intact brain slices rather than dissociated nuclei, it helps mitigate potential sampling biases inherent in single-nucleus profiling. Taken together, multiple lines of evidence indicate pronounced progenitor cell loss with aging.

Recent studies suggest that progenitor cell exhaustion in aging is driven by chromatin dysfunction, including loss of repressive histone marks and altered chromatin accessibility, rather than a simple failure of proliferation[28]. By integrating chromatin accessibility and transcriptional datasets across multiple independent approaches, including MERFISH (male), snATAC-seq (male), and 10x Multiome (female), we confirm consistent reductions in progenitor cell populations across replicates. To determine whether chromatin changes accompany progenitor depletion, we analyzed age-differentially accessible cis-regulatory elements (cCREs) in progenitor cell populations across age groups. Motif enrichment analysis revealed a significant depletion of homeobox motifs in OB-STR-CTX Inh IMN and Sox motifs in IOL_NN cells, indicating dysregulation of cell-identity transcription factors (Figure 2e). We focus on OB-STR-CTX Inh IMN due to their abundance in our data and their lack of characterization in published literature. Differential accessibility analysis revealed a progressive shift in chromatin accessibility with aging, with 9-month-old samples exhibiting an intermediate profile between young (2-month) and aged (18-month) states, suggesting a gradual rather than abrupt epigenomic transition during aging (Figure 2f). Lhx2 emerged as the most significantly downregulated transcription factor in OB-STR-CTX Inh IMN, with age-associated decreases in accessibility at Lhx2-motif sites (Figure 2g). Lhx2 is a key transcriptional regulator of neurogenic progenitors, maintaining their self-renewal capacity and delaying differentiation into mature neuronal or glial fates[29,30]. In embryonic and adult neural stem cells, Lhx2 prevents premature differentiation and supports ongoing neurogenesis, in part by directly activating downstream targets such as *Pax6*[29,31]. Consistent with this, differential gene expression analysis between 2-month-old and 18-month-old samples revealed that *Pax6*, a direct target of Lhx2 and a key regulator of neurogenic lineage specification[31], was significantly downregulated in both scRNA-seq and MERFISH data (adj p-value < 0.001, ~11.7 fold reduction in expression) (Figure 2j). *Pax6* is crucial for neural fate specification, and its age-related depletion underscores the progressive collapse of neurogenic potential. GO pathway enrichment analysis of genes differentially expressed between 2-month-old and 18-month-old samples revealed that those associated with learning, memory, and cell projection morphogenesis were downregulated with age (Figure 2i). Conversely, genes related to synapse organization were significantly

upregulated in these progenitors (Figure 2i), suggesting that a subset of cells may be prematurely differentiating. While progenitor depletion is a well-documented feature of aging, the upregulation of synaptic genes in the remaining OB-STR-CTX Inh IMN population may reflect a disruption in the balance between undifferentiated progenitors and early postmitotic neurons. This shift may be linked to the loss of Lhx2 and other homeobox transcription factors, which normally sustain the neurogenic program and suppress premature differentiation[30]. Together, these findings support a model in which age-related chromatin remodeling leads to the erosion of progenitor identity in OB-STR-CTX Inh IMN, in part through the progressive loss of Lhx2 and *Pax6* transcriptional regulation.

Dysregulation of cell identity genes in glial cells during aging

Having established the dramatic decline in progenitor populations, we next examined how aging affects the chromatin landscape of terminally differentiated cell types throughout the eight brain regions. We observed widespread transcriptional and chromatin accessibility changes in non-neuronal cell types, including oligodendrocytes, astrocytes, and microglia, which likely impact their ability to maintain brain homeostasis and support neuronal function. Dysfunction in these glial populations has been linked to neurodegenerative processes[32], underscoring the importance of understanding their regulatory changes with age.

To systematically examine chromatin accessibility changes in oligodendrocytes, we identified 1727 up-regulated and 2501 down-regulated differentially accessible candidate cis-regulatory elements (cCREs) across aging (Figure S4a). Chromatin accessibility changes in oligodendrocytes were consistent across brain regions and sexes and progressed gradually from 2 to 18 months (Figure 3a). Similarly to immature oligodendrocytes (IOLs), mature oligodendrocytes exhibit a decline in the activity of Sox transcription factors, which are crucial for maintaining oligodendrocyte identity (Figure 2e, 3b)[33]. Motif enrichment analysis revealed significant enrichment of Sox family and Creb5 motifs in downregulated cCREs, while KLF and SP family motifs were enriched in upregulated peaks, marking a shift in transcription factor activity (Figure 3b). These changes were further confirmed by aggregate plots of Klf1 and Sox6 motif presence in upregulated, downregulated, and non-changing peaks across brain regions (Figure 3c). Differential gene expression analysis (Figure 3d) revealed a downregulation of genes related to myelin sheath formation and energy production, while genes associated with synaptic organization were enriched in upregulated genes (Figure 3e). Previous studies have shown that oligodendrocytes express synaptic genes, which participate in axon-myelin communication[34]. In this context, the upregulation of synaptic organization genes in aging oligodendrocytes may reflect an adaptive response to maintain axon-glial interactions as neural circuits change with age. On the other hand, the downregulation of myelination related genes was evident across the 8 brain regions (Figure S8b,c). *Mal*, a gene that functions in recruitment of myelin protein in oligodendrocytes[35], is found to be significantly downregulated in oligodendrocytes from aged mice in both MERFISH and RNA-seq analysis (Figure 3h).

We linked these differential genes to key regulatory cCREs in oligodendrocytes using Activity-By-Contact (ABC) analysis[36], which predicts enhancer-promoter connections based on chromatin accessibility and genomic proximity. We calculated ABC scores using the snm3C-seq

contact data from our companion paper (Zeng et al.) and the accessibility data from our work in matching cell types. We found that Sox10 was the most significantly enriched transcription factor motif within peaks linked to downregulated genes in aging oligodendrocytes (Figure 3g). Sox10 is a master regulator of oligodendrocyte lineage progression and myelin gene expression, playing a critical role in maintaining oligodendrocyte function and promoting myelination[33]. While Sox transcription factors are well-established as essential regulators of oligodendrocyte development, our findings reveal that their downregulation in aging could contribute to the well-documented loss of myelination in aged brains[37,38]. This suggests that, in addition to being critical for early oligodendrocyte differentiation, Sox factors are important in maintaining myelination throughout life, highlighting a previously underappreciated role for these transcription factors in aging-related myelin decline. Beyond transcription factor activity dysregulation and downregulation of important functions like myelination, aging oligodendrocytes exhibit increased expression of genes involved in inflammatory and regulatory pathways, including lncRNA *Neat1*, Parkinson's disease driver gene *Snca*, and inflammatory marker *Il33* (Figure 3f). Collectively, these findings suggest that aging oligodendrocytes undergo chromatin and transcriptional changes that impair myelination, while the upregulation of synaptic and inflammatory genes, including *Snca* and *Il33*, may indicate a shift toward heightened responsiveness to neuronal and immune signals.

Astrocytes and microglia exhibit distinct shifts with aging, marked by increased accessibility at enhancers linked to stress-responsive transcription factors. Aging astrocytes from the frontal cortex exhibit the most age-dependent accessibility changes compared to other brain regions (Figure S4a). In these cells, cCREs gaining accessibility in aged mice are enriched for ATF(Zf) motifs, suggesting an adaptive response to the extracellular changes (Figure S4b). In contrast, cCREs gaining accessibility in aging microglia, particularly in microglia from the anterior hippocampus, exhibit IRF8 motif enrichment, indicating a shift toward a more pro-inflammatory, immune-activated state (Figure S4b). The upregulation of immune-related genes such as *Tnfsf8* and *Ildr2*, alongside the downregulation of classical microglial markers like C1qa and Cst3, suggests that aging microglia lose their cell identity while becoming chronically primed for inflammatory responses, a hallmark of neurodegeneration[1]. Previous studies have similarly reported that aging glial cells undergo transcriptional shifts marked by reduced activity of developmental transcription factors and increased expression of stress-responsive and immune-related genes[7,39–41]. Our brain-specific, multi-modal, and region-resolved analysis supports this model, revealing coordinated changes in chromatin accessibility and gene expression that underlie glial transcriptional reprogramming during aging.

Upregulation of AP-1 Mediated Transcriptional Programs in Aging Glutamatergic Neurons

Glutamatergic neurons, responsible for excitatory signaling in the brain, play a key role in cognition, synaptic plasticity, and neural circuit function. We found that aging induces widespread chromatin and transcriptional changes in these neurons, with distinct regional vulnerabilities (Figure S6). In dentate gyrus (DG) neurons, age-related chromatin remodeling exhibits clear regional specificity, with the anterior hippocampus (AHC) and posterior

hippocampus (PHC) showing divergent patterns of accessibility changes. Specifically, differential accessibility analysis identified 3,495 upregulated and 3,505 downregulated cCREs in aged DG neurons, with clusters of age-upregulated peaks enriched in the anterior hippocampus (AHC), while a distinct set of peaks showed greater downregulation in the posterior hippocampus (PHC) (Figure 4a). Motif enrichment analysis highlights regional differences in transcription factor activity, with CTCF motifs preferentially enriched in age-upregulated cCREs in the anterior hippocampus, suggesting altered chromatin looping and genome architecture in this region. Stress-responsive transcription factor complex AP-1 (Activator Protein 1) motifs are significantly upregulated in both brain regions (Figure 4b). Conversely, MEF2 motifs were strongly enriched in downregulated cCREs in the posterior hippocampus, suggesting a regional loss of transcriptional programs involved in synaptic plasticity and neuronal maintenance. MEF2 transcription factors regulate activity-dependent synapse remodeling and neuronal survival[40,42].

Genes involved in DNA damage response are upregulated in aging DG neurons while genes involved in axonogenesis are downregulated (Figure 4d,e). ABC analysis reveals that open chromatin regions linked to age-upregulated genes in these neurons are enriched for AP1 and CTCF motifs, while those associated with downregulated genes are enriched for NeuroG2 motifs (Figure 4f). This indicates a shift from developmental transcriptional programs toward stress-responsive regulatory networks during aging, where AP1 activation is a key driver of aging-related gene expression changes. This is consistent with recent findings demonstrating that AP-1 drives chromatin opening at stress-responsive cis-regulatory elements while cell identity transcription factor binding sites decline[7]. These findings highlight the regional specificity of chromatin remodeling in DG neurons, where the anterior hippocampus exhibits stronger stress responses and chromatin reorganization, while the posterior hippocampus experiences a greater loss of neurodevelopmental regulatory programs.

Beyond the hippocampus, glutamatergic neurons across multiple brain regions undergo extensive chromatin and transcriptional changes with aging. Motif enrichment analysis highlights an increase in open chromatin elements recognized by stress-responsive transcription factors, particularly KLF and AP1, suggesting that aging is associated with enhanced stress adaptation in glutamatergic neurons (Figure S6b). Conversely, MEF2 and RFX motifs are enriched in downregulated cCREs across aging neurons, indicating a loss of transcription factor binding at sites critical for neuronal development and synaptic maintenance (Figure S6b). CTCF motifs show strong enrichment in age-upregulated peaks across multiple regions, including the frontal cortex (FC), entorhinal cortex (ENT), and anterior hippocampus (AHC), further supporting widespread chromatin remodeling during aging (Figure S6b). Gene Set Enrichment Analysis (GSEA) reveals consistent downregulation of axonogenesis and oxidative phosphorylation pathways, suggesting a decline in synaptic plasticity and metabolic function across multiple glutamatergic neuron subtypes (Figure S12b, S13b). These transcriptional shifts align with previous findings that neuronal aging is marked by reduced bioenergetic capacity and neurogenesis[3]. Together, these findings demonstrate that glutamatergic neurons undergo significant age-related chromatin reorganization and transcriptional remodeling, with region-specific regulatory shifts in DG neurons and widespread stress responses across cortical regions.

Protocadherin Locus Derepression and Chromatin Remodeling in Aging Medium Spiny Neurons

GABAergic neuron populations play essential roles in inhibitory signaling across brain regions. With the exception of D12 medium spiny neurons (MSNs), which exhibit significant chromatin remodeling, most GABAergic subtypes show relatively modest chromatin and transcriptional changes with aging, though this may partially reflect lower cell numbers in our dataset (Figure S5a).

D12 medium spiny neurons (MSNs) are a key GABAergic subclass within the basal ganglia. This cell type is present in the caudate putamen (CP) and nucleus accumbens (NAC). We observed pronounced chromatin remodeling with aging in these cells. We further identified clusters of cCREs that are upregulated to higher levels in NAC and clusters of peaks more strongly downregulated in CP (Figure S9a). RFX motifs, which are involved in neuronal function[43] and are broadly enriched in downregulated peaks of many neuronal subtypes, are instead enriched in upregulated peaks of NAC (Figure S9b). AP-1 motifs show significant enrichment in upregulated peaks across both regions, mirroring broader trends in glutamatergic neurons, where AP-1 activation is associated with stress responses and transcriptional dysregulation (Figures S9b,S6b). Notably, the AP-1 motif signal is strongest in D12 MSNs, suggesting these neurons experience particularly high levels of aging-related stress.

Differential gene expression analysis across age revealed genes related to cell junction organization were significantly enriched in upregulated genes in aging, including Neuregulin (Nrg) family members and protocadherins such as *Pcdhgc5* (Figure S9c). One of the most striking chromatin changes in aging D12 MSNs is increased accessibility at the Protocadherin gamma (Pcdhg) and Protocadherin alpha (Pcdha) loci, gene clusters essential for neuronal self-recognition and synaptic organization[44]. While protocadherins exhibit differential expression across multiple cell types, D12 MSNs show the strongest alterations at this locus, present in both brain regions (Figure S5f). Notably, transcriptional upregulation within the Pcdhg cluster is largely intronic, suggesting that regulatory elements or noncoding RNAs within this region may be differentially expressed rather than the protein-coding genes themselves. Among these, *3222401L13Rik*, a long noncoding RNA within the Pcdhg locus that has recently been implicated in aging astrocytes[45], is upregulated across multiple cell types. 3C chromatin conformation data show structural changes at this locus, revealing increased contact frequency within the Pcdhg and Pcdha clusters while showing decreased interactions with upstream genomic regions (Figure S9e). These findings suggest that aging-induced chromatin reorganization in D12 MSNs may enhance protocadherin cluster activity while altering broader regulatory landscapes. The Pcdhg locus is part of a broader pattern of chromatin remodeling in aging neurons, where previously repressed genomic regions become more accessible. Recent studies have identified aging hotspots—genomic regions with significant accessibility gains—that overlap heterochromatin domains and are enriched in neurons[17]. In the next section, we examine the genome-wide consequences of heterochromatin loss, including transposable element activation, noncoding RNA upregulation, and stress-related reprogramming across cell types and brain regions.

Heterochromatin Destabilization, Transposable Element Activation, and lncRNA Dysregulation in Aging Brains

Beyond cell-type-specific changes, we identified broader chromatin reorganization patterns associated with aging across multiple cell types. We next examined how heterochromatin domains and transposable elements are affected during brain aging. In our previous work, we found that aging is accompanied by widespread chromatin remodeling, particularly at heterochromatin domains and transposable elements (TEs)[17], and aging neurons exhibit significant heterochromatin loss, particularly in cortical regions. With the increased resolution and broader scope of our current dataset spanning eight brain regions and multiple cell types, we now find that this phenomenon extends beyond neurons, with broad heterochromatin destabilization observed across diverse glial and neuronal populations. However, this effect remains most pronounced in glutamatergic neurons, particularly in the frontal cortex, hippocampus, entorhinal cortex, and amygdala, while the nucleus accumbens, periaqueductal gray, and caudate putamen exhibit little to no change (Figure S10).

To investigate heterochromatin alterations, we examined the overlap between age-associated differentially accessible regions and H3K9me3-marked heterochromatin domains from mouse forebrain[46] (Methods). Age-upregulated peaks were significantly enriched in H3K9me3 domains, particularly in glutamatergic neurons (Figure 5a, middle), suggesting that aging is associated with the erosion of heterochromatin integrity. Consistent with this, transposable elements exhibited a pronounced shift toward increased accessibility across multiple cell types (Figure 5a, right), with specific subfamilies showing consistent patterns of activation across cell types (Figure S12c). This trend was evident in both male and female mice (Figure S10b), reinforcing heterochromatin erosion as a conserved feature of brain aging. Motif enrichment analysis revealed differentially upregulated regions within heterochromatin that were enriched for pioneer transcription factor AP1 family (bZIP)[47] and CTCF motifs (Figure 5b).

Using Gaussian density scoring, a computational approach to identify genomic regions with significantly higher-than-expected concentrations of differential accessibility[17] (Methods), we identified chromosomal aging hotspots across the genome. These hotspots were particularly upregulated in glutamatergic neurons, especially in cortical and hippocampal regions (Figure 5c). Notably, 47% of significantly upregulated hotspots overlap H3K9me3-marked domains, despite these regions covering only ~3% of the genome in these brain cells. This strong association between aging-associated accessibility gains and constitutive heterochromatin suggests a widespread breakdown of repressive chromatin compartments during aging. Many of these hotspots correspond to intergenic regions with TE activities, gene clusters that are typically repressed in mature neurons, and lncRNAs (Figure S3). Notably, lncRNAs were overrepresented among the most differentially expressed genes in aging, with over 50% of the top 100 upregulated genes in some cortical neuron cell types belonging to this category (Figure 5g). One of the most prominent aging-associated hotspots is located at the start of chromosome 13, where accessibility gains were observed across five brain regions (Figure 5e). This region contains the lncRNA *Gm48530*, which was the most significantly upregulated gene in aging cortical neurons across the same five brain regions (Figure 5d). The hotspot also overlaps

IAPLTR3-int, a TE element that exhibited increased accessibility in multiple cell types (Figure 5h, S12c). Together, this locus exhibited coordinated increases in chromatin accessibility, gene expression, and hypomethylation (Figure 5h), suggesting that age-related chromatin remodeling at heterochromatin domains may alter regulatory landscapes and lead to transcriptional activation.

Beyond autosomal hotspots, several aging-associated hotspots were found in the X chromosome in female samples (Figures S11a, S3). The most significant of these occurred at the Firre lncRNA locus, which exhibited continuous and drastic accessibility increases (Figure S11a). This finding aligns with previous reports linking aging to the loss of X chromosome inactivation[48–50]. Similarly, the lncRNA *Dxz4*, another key element involved in X chromosome organization, exhibited increased accessibility in aging neurons, suggesting that large-scale shifts in X-linked chromatin architecture may accompany aging (Figure S11a). In parallel, Xist and Tsix, two critical regulators of X chromosome inactivation, were among the most differentially-upregulated genes across multiple female brain regions and cell types, especially in neurons, consistent with previous research (Fig. S11c)[49]. This could be a compensatory mechanism to counteract the possible loss of X chromosome inactivation we observe. Interestingly, while the *Firre* and *Dxz4* loci gained accessibility with age, the pseudoautosomal region at the end of the X chromosome, which typically escapes X inactivation, exhibited a striking loss of chromatin accessibility and gene expression in female mice (Figure S11a, b). The most affected region included *Erdr1* (*Gm47283*), which was the most consistently downregulated lncRNA in female brain aging across cell types and brain regions. This opposing pattern—decreased accessibility at normally active X-linked regions alongside increased accessibility at heterochromatin-associated loci - suggests that chromosome X undergoes extensive chromatin reorganization in aging females, potentially reflecting an extension of global heterochromatin destabilization.

Currently, the mechanisms responsible for the aging associated heterochromatin decay remain unclear. We noted that among the most consistently down-regulated pathways across cell types was oxidative phosphorylation (Figure S13a,b), highlighting the central role of metabolic decline in brain aging. This was particularly pronounced in neuronal populations, where energy demands are highest[51]. Genes involved in protein synthesis were also broadly downregulated, consistent with reduced energy availability in these cells. Additionally, we observed downregulation of genes involved in heterochromatin maintenance (Figure S13c), including histone methyltransferases and chromatin remodeling factors, providing a potential mechanistic explanation for the heterochromatin instability observed across cell types. These findings highlight heterochromatin remodeling, TE activation, and lncRNA dysregulation as key hallmarks of aging in the brain. The widespread loss of heterochromatin integrity, coupled with transcriptional shifts in chromatin organization and increased TE activity, suggests that aging involves a progressive breakdown of epigenetic regulatory barriers. This dysregulation may contribute to genomic instability and functional decline in aging neurons, underscoring the need for further investigation into chromatin-based mechanisms of neurodegeneration.

Discussion

We show here that aging is accompanied by profound changes in chromatin accessibility, transcription factor activity, and cell identity maintenance in the brain. Our multi-omic analysis across eight brain regions reveals key regulatory features underlying these changes, linking master transcription factor loss, stress-induced reprogramming, and heterochromatin instability to cellular dysfunction in aging.

A major hallmark of aging observed in our data is the decline of transcription factors crucial for cell identity and function. In progenitor populations, factors such as *Lhx2* and *Pax6* show significant reductions, impairing neurogenic capacity. Similarly, oligodendrocytes and their precursors (IOLs) exhibit downregulation of *Sox* genes, disrupting myelination and oligodendrocyte maintenance. In neurons, master transcription factors including *Mef2* and *NeuroG2* lose function, likely contributing to deficits in axonogenesis and synaptic plasticity, as seen in downregulated genes. As lineage-specific, developmental transcription factors decline, aging cells exhibit an upregulation of stress-responsive transcription factors. We observe increased accessibility of motifs for AP1 (bZIP) in neurons, KLF across cell types, and IRF8 in microglia, linking aging to inflammation, oxidative stress, and immune activation.

Another key feature of aging shown in our data is the widespread loss of heterochromatin integrity, accompanied by dysregulation of transposable elements (TEs) and non-coding RNAs. Long noncoding RNAs (lncRNAs) are among the most upregulated genes, particularly those located within heterochromatin-associated domains. Aging hotspots overlapping heterochromatin regions are consistently observed across autosomes in both male and female mice. However, female mice uniquely exhibit increased chromatin accessibility on the X chromosome, alongside a concurrent loss of accessibility and expression at the pseudo-autosomal region. These findings suggest that aging-driven chromatin reorganization extends beyond autosomal heterochromatin erosion, affecting large-scale X-linked regulatory landscapes in a sex-specific manner. This dimorphism in X chromosome regulation may contribute to known sex differences in brain aging trajectories and neurodegeneration susceptibility, though the functional consequences require further investigation.

Our data suggest that aging is associated with a loss of transcriptional and epigenetic control over cell identity, causing cells to drift away from their defined states. The concurrent loss of developmental transcription factors, increased stress response activity, and heterochromatin breakdown contribute to a landscape where regulatory control is progressively lost. In this context, our findings align with emerging models of aging that propose a loss of epigenetic constraints leading to transcriptional drift[7,52]. The reactivation of TEs and lncRNAs, coupled with downregulation of genes important to metabolic and cellular function, suggests that aging cells fail to maintain repression of elements that should remain silenced while also struggling to sustain essential transcriptional programs critical for homeostasis and function.

Epigenetic and transcriptional interventions have shown promise in mitigating aging-related decline, and our findings provide a mechanistic context for these approaches. The widespread loss of heterochromatin integrity in aging neurons aligns with studies showing that reinforcing heterochromatin maintenance can extend lifespan and preserve cellular function[53,54]. Similarly, the depletion of lineage-defining transcription factors suggests that stabilizing these networks

could counteract the progressive loss of cell identity with age. Reprogramming with pluripotency factors has been shown to reverse aspects of cellular aging[8,55] yet the underlying mechanisms remain unclear. Our findings suggest that aging brain cells lose regulatory control, shifting from developmental transcription factor networks toward stress-related reprogramming. Future efforts should focus on targeted strategies to reinforce lost transcriptional programs and maintain heterochromatin, with the goal of preserving cognitive function and delaying neurodegeneration.

Limitations of the study

This study captures key chromatin and transcriptional changes across aging but is limited to three timepoints, which may not fully resolve the temporal dynamics of regulatory decline. The 18-month timepoint reflects mid-to-late adulthood in mice, not extreme old age. Sex-specific analyses are constrained by differing methodologies between sexes (snATAC-seq in males, 10X Multiome in females), limiting direct comparisons. Finally, the findings are correlative; causal relationships between transcription factor dysregulation, chromatin remodeling, and aging phenotypes remain to be tested through perturbation studies.

Resource Availability

Lead Contact

Further information and requests for resources and reagents should be directed to Bing Ren (biren@ucsd.edu) and M Marga Behrens (mbehrens@salk.edu).

Materials Availability

This study did not generate new unique reagents.

Data and Code Availability

The raw data from this study have been deposited in SRA under project number PRJNA1248586. The processed data from this study have been deposited in the NCBI's Gene Expression Omnibus (GEO) database under accession number GSE294772. Analysis codes are available on GitHub at https://github.com/luisajamaral/aging_mouse_brain_code. Any additional information needed to reanalyze the data reported in this paper can be obtained from the lead contact upon request.

Acknowledgments

This work was supported by the National Institutes of Health (NIH) grant 5R01AG066018 to B.R, M.M.B and J.R.E.

Author Contributions

B.R., J.R.E., M.M.B., and M.L.A. conceived and designed the study. M.L.A. performed analysis and drafted the manuscript. J.Osteen, A.B., J.R., N.D.J., and S.Ca. contributed

to tissue dissection and nuclei production. M.M., Q.Y., E.E., and E.W.S. generated the 10x Multiome data. X.H. generated the snATAC-seq data. A.W. oversaw data generation for scATAC and 10X Multiome data. C.T.B.B., J.A., S.C., N.E., and J.L. generated MERFISH data. J.Olness. and C.K. preprocessed the MERFISH data under the supervision of Q.Zhu. Q.Z. analyzed shared snm3c-seq data and calculated ABC scores. S.M. performed RNA doublet removal. S.Z. provided datasets for label transfer. M.L.A., S.M., and T.L. managed public data release. J.R.E., M.M.B., M.L.A., and B.R. coordinated the research and edited the manuscript. B.R. supervised the data collection and analysis.

Declaration of Interests

B.R. is a co-founder and consultant of Arima Genomics, Inc., and a co-founder of Epigenome Technologies Inc.

Main Figures

Figure 1. Single-nucleus multi-omic atlas of brain aging across eight regions in the mouse.
(A) Schematic of experimental design showing brain regions profiled from male and female mice at 2, 9, and 18 months of age using snATAC-seq, 10X Multiome, and MERFISH.
(B) Uniform Manifold Approximation and Projection (UMAP) of single-nucleus ATAC-seq (left), RNA-seq (center), and MERFISH (right) datasets, annotated by cell type.
(C) Weighted cell-type proportions across ages for each modality, highlighting three progenitor populations that decline with age.
(D) Statistical significance of age-associated changes in cell-type proportions (Wilcoxon rank-sum test).

Figure 2. Aging depletes progenitor populations and disrupts neurogenic regulatory programs.
(A) MERFISH spatial maps of brain slices (plates 46 and 69) with cells colored by annotated cell types (Table S1).
(B) Representative MERFISH images across three ages showing immature oligodendrocytes (IOL), OB-STR-CTX inhibitory immature neurons (Inh IMN), and dentate gyrus (DG) progenitors.
(C) Age-associated changes in progenitor cell-type proportions from MERFISH data.
(D) Progenitor cell-type proportions from snATAC-seq across brain regions and sexes.
(E) Motif enrichment analysis of age-associated differentially accessible cCREs in progenitor populations.
(F) Heatmap showing normalized accessibility (z-score) of age-differential cCREs in OB-STR-CTX Inh IMN, stratified by age and sex.
(G) Proportion of downregulated cCREs containing Lhx2 motifs in OB-STR-CTX Inh IMN; bottom shows the Lhx2 consensus motif.
(H) MA plot of age-differential gene expression (18 mo vs. 2 mo) in OB-STR-CTX Inh IMN.
(I) GO term enrichment for upregulated (top) and downregulated (bottom) genes in OB-STR-CTX Inh IMN.

(J) Age-associated expression of *Pax6*, a direct target of Lhx2, in scRNA-seq (top) and MERFISH (bottom) datasets.

Figure 3. Aging oligodendrocytes exhibit transcriptional and chromatin changes associated with myelination loss and Sox factor decline.
(A) Heatmap showing normalized accessibility (z-score) at age-differential cCREs in oligodendrocytes across brain regions and sexes.
(B) Motif enrichment of downregulated (left) and upregulated (right) age-differential cCREs in oligodendrocytes; asterisks denote significance (adjusted $p < 0.01$).
(C) Aggregate motif accessibility plots for Klf1 and Sox6 in upregulated, downregulated, and non-changing peaks in oligodendrocytes (Oligo NN).
(D) MA plot of age-differential gene expression (18 mo vs. 2 mo) in oligodendrocytes.
(E) GO term enrichment analysis for upregulated (top) and downregulated (bottom) genes.
(F) Bar plot showing average age log fold-change of gene expression for downregulated, non-significant, and upregulated genes, with corresponding changes in linked peaks from ABC score analysis.
(G) Motif logos for the most enriched motifs in peaks linked to upregulated (top) and downregulated (bottom) genes in aging oligodendrocytes.
(H) Age-associated expression of the myelination gene *Mal* from scRNA-seq (left) and MERFISH (right).

Figure 4. Aging induces region-specific regulatory reprogramming in dentate gyrus glutamatergic neurons
(A) Heatmap of normalized chromatin accessibility (z-score) at age-differential cCREs in dentate gyrus (DG) neurons across brain regions.
(B) Motif enrichment analysis of downregulated (left) and upregulated (right) age-differential cCREs using all peaks as background; asterisks denote significance (adjusted $p < 0.01$).
(C) Aggregate accessibility plots of AP-1 and CTCF motifs at upregulated, downregulated, and all cCREs across DG neuron regions.
(D) MA plot of age-differential gene expression between 2-month-old and 18-month-old DG neurons.
(E) Gene Ontology (GO) enrichment analysis of genes upregulated with age.
(F) Bar plot showing mean age $\log_2$ fold change of downregulated, non-significant, and upregulated genes, along with corresponding changes in linked cCREs from ABC analysis. Right: Motif logos for the most enriched motifs in peaks linked to up- and downregulated genes.

Figure 5. Upregulated accessibility and transcriptional shifts within heterochromatin-associated genomic hotspots.
(A) Differentially accessible regions (DARs) in aging neurons. Left: Non-H3K9me3 peaks show a balanced distribution of up- and downregulated peaks. Middle: H3K9me3-overlapping peaks are predominantly upregulated, especially in glutamatergic neurons. Right: Transposable element (TE) subfamilies show widespread age-related increases in accessibility.
(B) Motif enrichment analysis of age-upregulated DARs across neuronal populations.
(C) Genomic hotspots with higher-than-expected density of DARs across cell types, colored by overlap with H3K9me3 domains.
(D) $\log_2$ fold change and significance of lncRNA *Gm48530* expression across brain regions, located within an aging hotspot.
(E) Chromosomal hotspot on chromosome 13 across brain regions; each point represents a cell type, colored by cell type clade.

(F) Age-related transcriptional changes from scRNA-seq. Left: $\log_2$ fold change of genes across cell types, highlighting *Gm48530* among the most significantly upregulated. Right: TE subfamily expression shows a broader trend of upregulation.
(G) Proportion of the top 100 most upregulated and downregulated genes that are long noncoding RNAs or pseudogenes.
(H) Genome browser view of the chromosome 13 hotspot, including *Gm48530* and IAPLTR3-int, showing increased accessibility, expression, and hypomethylation with age.

Supplementary Figures

Figure S1. Characterization of multi-omic datasets and age-related gene regulation.
(A) Cell type color legend corresponding to Figures 1B and 2A.
(B) UMAP of snATAC-seq data annotated by sex.
(C) UMAP of snATAC-seq data annotated by brain region.
(D-F) UMAP projections of scATAC-seq, scRNA-seq, and MERFISH data colored by age group (2mo, 9mo, 18mo).
(G) Number of cells per celltype for ATAC data (male and female)

Figure S2. Cell type-level peak calling identifies cell-type-specific regulatory signatures.
(A) Number of peaks called by MACS3 per cell type, colored by genomic annotation.
(B) Heatmap showing accessibility ($\log_2$[1 + RPKM]) at marker cis-regulatory elements (cCREs) across cell types.

Figure S3. Genome-wide locations of age-associated chromatin accessibility changes in male and female brains.
(A) Genomic locations of age-upregulated differentially accessible regions (DARs), plotted as $\log_2$ fold change (18mo/2mo) across chromosomes.
(B) Genomic locations of age-downregulated DARs, plotted as $\log_2$ fold change (2mo/18mo) across chromosomes.

Figure S4. Aging-associated chromatin and transcriptional changes in non-neuronal cell types.
(A) Left to right: Cell counts per non-neuronal cell type, brain region, and modality. Bar plot showing the number of age-associated DARs (adj. $p < 0.01$, $|\log_2 FC| > 0.25$). Scatter plots of $\log_2$ fold change ($\log_2 FC$) for DARs, colored by direction (up- or downregulated with age). Bar plot showing the number of age-associated DEGs (adj. $p < 0.01$, $|\log_2 FC| > 0.25$).
(B) Motif enrichment in age-DARs across non-neuronal cell types. Dot size indicates $-\log_{10}$(p-value), and color denotes direction of change with aging.

Figure S5. Aging-associated chromatin and transcriptional changes in GABAergic cell types.
(A) Left to right: Cell counts per GABAergic cell type, brain region, and modality. Bar plot showing the number of age-associated DARs (adj. $p < 0.01$, $|\log_2 FC| > 0.25$). Scatter plots of $\log_2$ fold change ($\log_2 FC$) for DARs, colored by direction (up- or downregulated with age). Bar plot showing the number of age-associated DEGs (adj. $p < 0.01$, $|\log_2 FC| > 0.25$). Scatter plots of $\log_2 FC$ for DEGs, colored by direction of change.

(B) Motif enrichment in age-DARs across GABAergic cell types. Dot size indicates $-\log_{10}$(p-value), and color denotes direction of change with aging.

Figure S6. Aging-associated chromatin and transcriptional changes in glutamatergic cell types.
(A) Left to right: Cell counts per glutamatergic cell type, brain region, and modality. Bar plot showing the number of age-associated DARs (adj. $p < 0.01$, $|\log_2 FC| > 0.25$). Scatter plots of $\log_2$ fold change ($\log_2 FC$) for DARs, colored by direction (up- or downregulated with age). Bar plot showing the number of age-associated DEGs (adj. $p < 0.01$, $|\log_2 FC| > 0.25$). Scatter plots of $\log_2 FC$ for DEGs, colored by direction of change.
(B) Motif enrichment in age-DARs across glutamatergic cell types. Dot size indicates $-\log_{10}$(p-value), and color denotes direction of change with aging.

Figure S7. Cross-modal correlation of gene expression across cell types.
(A) Heatmap showing Pearson correlation coefficients between RNA-seq and MERFISH gene expression profiles across shared cell types. Expression values were CLR-normalized per cell, aggregated by cell type, and RNA-seq values were additionally normalized by gene length. Correlations were computed across shared genes to assess concordance between modalities.

Figure S8. Downregulation of myelination-associated genes in aging oligodendrocytes.

(A) Genome browser tracks showing chromatin accessibility (male ATAC, female ATAC) and RNA expression (female RNA) across age in eight brain regions in oligodendrocytes at the age-associated gene C4b.
(B) Heatmap of the top 30 age-associated DEGs in oligodendrocytes, showing consistent downregulation of genes enriched for the “myelin sheath” GO term across brain regions.
(C) MA plots of DEGs in oligodendrocytes, highlighting myelination-related genes (*Mal*, *Mog*, *Olig1*). X-axis denotes the percentage of cells expressing each gene; Y-axis shows $\log_2$ fold change (18mo vs. 2mo).

Figure S9. Aging-associated chromatin remodeling and protocadherin locus reorganization in D12 MSN neurons.

(A) Heatmap showing scaled, normalized chromatin accessibility at age-differential cCREs in D12 medium spiny neurons (MSNs) from the striatum.
(B) Motif enrichment analysis for age-upregulated and age-downregulated cCREs in D12 MSNs.
(C) MA plot of age-differentially expressed genes (DEGs) in D12 MSNs (18mo vs. 2mo).
(D) GO Biological Process enrichment for age-upregulated (left) and age-downregulated (right) DEGs.
(E) Genome browser view of the *Protocadherin gamma* (Pcdhg) gene cluster in D12 MSNs showing increased chromatin accessibility, gene expression, hypomethylation, and altered Hi-C contact frequency with aging.
(F) Heatmap of normalized expression levels for *Pcdhg* genes across age groups and brain regions in D12 MSN GABAergic neurons.
(G) Zoomed-in IGV view of the *Pcdhg* locus highlighting specific aging-associated regulatory changes.

Figure S10. Chromosomal aging hotspots and heterochromatin loss across brain regions.
(A) Chromosomal aging hotspots with significantly more DARs than expected by chance across cell types. Points are colored by cell type clade (glutamatergic, GABAergic, non-neuronal) and faceted by brain region, highlighting regions of age-associated chromatin accessibility gain or loss.
(B) Volcano plots of differential chromatin accessibility within H3K9me3-marked domains across brain regions for glutamatergic, GABAergic, and non-neuronal cells. X-axis: $\log_2$ fold change (18mo/2mo); Y-axis: $-\log_{10}$(adjusted p-value). Point size represents the length of the H3K9me3 domain.

Figure S11. Sex chromosome aging hotspots and pseudoautosomal region remodeling.
(A) Aging-associated chromatin accessibility hotspots on the sex chromosomes. Highlighted region at the distal end of chromosome Y corresponds to the pseudoautosomal region.
(B) Genome browser view (IGV) of the pseudoautosomal region containing *Erdr1* (also known as *Gm47283*) across representative cell type STR_D12_GABA, showing chromatin accessibility (male ATAC, female ATAC) and RNA expression (female RNA) across age groups.
(C) Heatmap of age-related $\log_2$ fold change (18mo/2mo) in expression for pseudoautosomal region genes (*Gm47283*, *Mid1*) and X-inactivation regulators (*Xist*, *Tsix*) across major cell types.

Figure S12. Top aging-associated regulatory and transcriptional changes across cell types.
(A) Motif enrichment analysis of age-associated differentially accessible regions (age-DARs), showing top enriched transcription factor motifs across cell types.
(B) Gene Ontology (GO) pathway enrichment analysis of age-associated differentially expressed genes (age-DEGs), highlighting recurrent biological processes altered with aging.
(C) Top differentially accessible transposable element (TE) subfamilies across aging, ranked by frequency and magnitude of accessibility changes.

Figure S13. Aging-associated downregulation of oxidative phosphorylation and heterochromatin maintenance genes.
(A) MA plots highlighting age-associated downregulated genes (18mo vs. 2mo) related to oxidative phosphorylation across brain regions.
(B) Heatmap showing $\log_2$ fold change ($\log_2$FC) in expression of top oxidative phosphorylation-related genes across major cell types.
(C) Heatmap showing $\log_2$FC in expression of genes involved in heterochromatin maintenance, indicating widespread transcriptional decline of chromatin regulators with aging.

Methods

Mouse brain tissue

All experimental procedures using live animals were performed at the Salk Institute, and were approved by the Animal Care and Use Committee (IACUC). The Salk Institute has approved Assurance from NIH Office of Protection from Research Risks (D16-00328). C57BL/6J male and female mice were purchased from the Jackson Laboratory at 7, 38 and 63 weeks of age

and maintained in the Salk animal barrier facility on 12-h dark–light cycles with food ad libitum until brain extraction (housing conditions: temperature of 21–23 °C, relative humidity of 61–63%). For synchronizing the estrous cycle in females ahead of brain extraction, females were exposed to male bedding for three days such that they would be in di-estrous at time of dissection. All animals were dissected between 1 and 5 pm to ensure similarity of circadian rhythm. Brains were extracted at 2, 9 or 18 months of age, sliced coronally at 600 µm and regions dissected in an ice-cold dissection buffer as previously described[56] according to the Allen Brain Reference Atlas CCF (version 3)[56](CCFv3). Dissected tissue corresponding to the same region (across the anterior posterior axis) from each animal was collected across brain slabs and stored at -80 ºC. For nuclei isolation, region pools from 3–14 animals were processed for each of 2–3 biological replicas per region. Comprehensive brain dissection metadata are provided in Table S1. No statistical methods were used to predetermine sample sizes. We empirically determined the number of animals needed to obtain sufficient nuclei from each brain region to run single nuclei sequencing experiments. We use two to three biological replicas for all single-cell epigenomic experiments to achieve minimum reproducibility for large-scale projects. Blinding and randomization was not performed during handling of the tissue samples. Additionally, all dissected regions were previously digitally registered into CCFv3 using ITK-SNAP[56] (v.4.0.0) at 25 µm resolution.

Single-nucleus ATAC-seq data generation

Combinatorial barcoding single-nucleus ATAC-seq was provided by the Center for Epigenomics, UC San Diego and performed as previously described[57–59]. Briefly, for each sample, tissue from 8 brain regions (AMY, CP, ENT, RLP, NAC, AHC, PHC, FC -- See Supplementary Table 1 for dissection information) was homogenized using mortar and pestle on liquid nitrogen. 1 ml nuclei permeabilization buffer (10 mM Tris-HCL [pH 7.5], 10 mM NaCl, 3 mM MgCl2, 0.1% Tween-20 [Sigma], 0.1% IGEPAL-CA630 [Sigma] and 0.01% Digitonin [Promega] in water; Corces et al., 2017) was added to 30 mg of ground lung tissue and tissue was resuspended by pipetting for 8–15 times. Nuclei suspension was incubated for 10 min at 4°C and filtered with 30 µm filter (CellTrics). Nuclei were pelleted with a swinging bucket centrifuge (500 x g, 5 min, 4°C; 5920R, Eppendorf), resuspended in 500 µL high salt tagmentation buffer (36.3 mM Tris-acetate (pH = 7.8), 72.6 mM potassium-acetate, 11 mM Mg-acetate, 17.6% DMF) and counted using a hemocytometer. Concentration was adjusted to 2000 nuclei/9 µL, and 2000 nuclei were dispensed into each well of one 96-well plate. For tagmentation, 1 µL barcoded Tn5 transposomes[60] was added using a BenchSmart 96 (Mettler Toledo), mixed five times and incubated for 60 min at 37°C with shaking (500 rpm). To inhibit the Tn5 reaction, 10 µL of 40 mM EDTA were added to each well with a BenchSmart 96 (Mettler Toledo) and the plate was incubated at 37°C for 15 min with shaking (500 rpm). Next, 20 µL 2 x sort buffer (2% BSA, 2 mM EDTA in PBS) was added using a BenchSmart 96 (Mettler Toledo). All wells were combined into a FACS tube and stained with 3 µM Draq7 (Cell Signaling). Using a SH800 (Sony), 20 2 n nuclei were sorted per well into eight 96-well plates (total of 768 wells) containing 10.5 µL EB (25 pmol) primer i7, 25 pmol primer i5, 200 ng BSA (Sigma). Preparation of sort plates and all downstream pipetting steps were performed on a Biomek i7 Automated Workstation (Beckman Coulter). After addition of 1 µL 0.2% SDS, samples were incubated at

55°C for 7 min with shaking (500 rpm). 1 µL 12.5% Triton-X was added to each well to quench the SDS. Next, 12.5 µL NEBNext High-Fidelity 2 × PCR Master Mix (NEB) were added and samples were PCR-amplified (72°C 5 min, 98°C 30 s, (98°C 10 s, 63°C 30 s, 72°C 60 s)×12 cycles, held at 12°C). After PCR, all wells were combined. Libraries were purified according to the MinElute PCR Purification Kit manual (Qiagen) using a vacuum manifold (QIAvac 24 plus, Qiagen) and size selection was performed with SPRI Beads (Beckmann Coulter, 0.55x and 1.5x). Libraries were purified one more time with SPRI Beads (Beckmann Coulter, 1.5x). Libraries were quantified using a Qubit fluorimeter (Life technologies) and the nucleosomal pattern was verified using a Tapestation (High Sensitivity D1000, Agilent). The library was sequenced on a NovaSeq6000 or NextSeq500 sequencer (Illumina) using custom sequencing primers with following read lengths: 50 + 10 + 12 + 50 (Read1 + Index1 + Index2 + Read2).

Single-nucleus RNA-seq data generation

Single nucleus RNA-seq was provided by the Center for Epigenomics, UC San Diego using the Droplet-based Chromium Single-Cell 3' solution (10x Genomics, v3 chemistry)[61]. Briefly, 30 mg pulverized tissue , tissue from 8 brain regions (AMY, CP, ENT, RLP, NAC, AHC, PHC, FC) was resuspended in 500 µL of nuclei permeabilization buffer (0.1% Triton-X-100 (Sigma-Aldrich, T8787), 1X protease inhibitor, 1 mM DTT, and 0.2 U/µL RNase inhibitor (Promega, N211B), 2% BSA (Sigma-Aldrich, SRE0036) in PBS). Sample was incubated on a rotator for 5 min at 4°C and then centrifuged at 500 rcf for 5 min (4°C, run speed 3/3). Supernatant was removed and pellet was resuspended in 400 µL of sort buffer (1 mM EDTA 0.2 U/µL RNase inhibitor (Promega, N211B), 2% BSA (Sigma-Aldrich, SRE0036) in PBS) and stained with DRAQ7 (1:100; Cell Signaling, 7406). 75,000 nuclei were sorted using a SH800 sorter (Sony) into 50 µL of collection buffer consisting of 1 U/µL RNase inhibitor in 5% BSA; the FACS gating strategy sorted based on particle size and DRAQ7 fluorescence. Sorted nuclei were then centrifuged at 1000 rcf for 15 min (4°C, run speed 3/3) and supernatant was removed. Nuclei were resuspended in 35 µL of reaction buffer (0.2 U/µL RNase inhibitor (Promega, N211B), 2% BSA (Sigma-Aldrich, SRE0036) in PBS) and counted on a hemocytometer. 12,000 nuclei were loaded onto a Chromium Controller (10x Genomics). Libraries were generated using the Chromium Single-Cell 3′ Library Construction Kit v3 (10x Genomics, 1000075) with the Chromium Single-Cell B Chip Kit (10x Genomics, 1000153) and the Chromium i7 Multiplex Kit for sample indexing (10x Genomics, 120262) according to manufacturer specifications. CDNA was amplified for 12 PCR cycles. SPRISelect reagent (Beckman Coulter, B23319) was used for size selection and clean-up steps. Final library concentration was assessed by Qubit dsDNA HS Assay Kit (Thermo-Fischer Scientific) and fragment size was checked using Tapestation High Sensitivity D1000 (Agilent) to ensure that fragment sizes were normally distributed about 500 bp. Libraries were sequenced using the NextSeq500 and a NovaSeq6000 (Illumina) with these read lengths: 28 + 8 + 91 (Read1 + Index1 + Read2).

Nuclei Preparation from Frozen Organoids for 10X Multiome

Frozen organoids were processed to isolate nuclei using dounce homogenization. Briefly, organoids were suspended in 1 mL of nuclei permeabilization buffer (0.1% Triton-X-100 (Sigma-Aldrich, T8787), 1X protease inhibitor, 1 mM DTT, and 0.2 U/µL RNase inhibitor (Promega,

N211B), 2% BSA (Sigma-Aldrich, SRE0036) in PBS) and transferred to a pre-chilled Dounce homogenizer. Homogenization was carried out first using the loose pestle (5–10 strokes), followed by the tight pestle (15–25 strokes) until organoids were uniformly disrupted. The homogenate was filtered through a 30 µm filter and centrifuged at 1000 × g for 10 min at 4°C. The supernatant was discarded, and the pellet was resuspended in 1 mL of nuclei permeabilization buffer. After a second centrifugation, the pellet was resuspended in 400 µL of Sort Buffer (1 mM EDTA 1 U/µL RNase inhibitor (Promega, N211B), 2% BSA (Sigma-Aldrich, SRE0036) in PBS) and incubated with 7-AAD (2 µM) on ice for 10 min. Nuclei were sorted, and 120,000 nuclei were collected in 87.5 µL of collection buffer (1 U/µL RNase inhibitor (Promega, N211B), 2% BSA (Sigma-Aldrich, SRE0036) in PBS). The nuclei were incubated on ice for 1 min, centrifuged (500 × g for 5 min at 4°C), and washed twice with Wash Buffer. The final nuclei suspension was resuspended in 10 µL of 1X Nuclei Buffer, and nuclei were counted using a hemocytometer after staining with Trypan Blue. A total of 18,000 nuclei were loaded per tagmentation reaction loaded onto a Chromium Controller (10x Genomics) for downstream 10X Multiome ATAC and gene expression workflows. Final library concentration was assessed by Qubit dsDNA HS Assay Kit (Thermo-Fischer Scientific) and fragment size was checked using Tapestation High Sensitivity D1000 (Agilent) to ensure that proper fragment sizes. Libraries were sequenced using the NextSeq500 and a NovaSeqX plus (Illumina).

snATAC-seq Data Processing

Reads were aligned to the mm10 reference genome using bowtie2 (v2.3)[62] with default parameters and cell barcodes were added as a BX tag in the bam file. Only primary alignments were kept. Then we removed duplicated read pairs with Picard. Only proper read pairs with insert size less than 2000 were kept for further analysis. From the filtered BAM files, we processed the data using SnapATAC2 (v 2.5.1)[20], following the official SnapATAC2 documentation. Barcode processing and fragment generation were performed, and doublets were removed using Scrublet[63]. Nuclei with fewer than 1,000 fragments, more than 100,000 fragments, or a TSS enrichment score below 5 were discarded. For female 10X Multiome samples, we processed the CellRanger output directly using SnapATAC2, ensuring consistency between modalities. Fragment files were imported, and doublets were identified and removed using SnapATAC2's built-in method. TSS enrichment scores were computed using SnapATAC2’s function, and cells with fewer than 1,000 fragments, more than 15,000 fragments, or a TSS enrichment score below 5 were removed. Read counting and clustering were performed using a cell-by-bin matrix at 500-bp resolution, which was binarized for clustering. Bins overlapping the ENCODE[64] blacklist (mm10) were removed to eliminate problematic regions. Read coverage normalization was performed using a log10(count +1) transformation followed by Z-score scaling, and bins with extreme Z-scores greater than 2 were filtered out. Feature selection was performed by retaining the top 700,000 most variable features. For dimensionality reduction, the Jaccard Index was computed, followed by diffusion maps for embedding. The top 20 eigenvectors were selected based on variance explained, and 20 nearest neighbors were computed per nucleus. The Leiden algorithm was applied for clustering, and clusters were annotated using known marker genes. Batch effects between male and

female samples were corrected using Harmony[21] prior to clustering. Low-quality clusters, including those with low TSS enrichment or suspected doublets, were removed from downstream analysis.

snRNA-seq Data Processing

Single-nucleus RNA-seq (snRNA-seq) data were generated using the 10X Genomics Multiome platform and processed with Cellranger-arc v2.0.2 to generate raw gene expression matrices[61]. Doublets were identified and removed using DoubletFinder from the Cell Ranger output for each sample[65]. Downstream analysis was performed using Seurat v5 in R. Individual samples were then merged into a single Seurat object. Quality control was applied to remove low-quality nuclei, filtering out cells with fewer than 500 or more than 6000 detected genes, and cells with >10% mitochondrial reads. Normalization was performed using the SCTransform (SCT) workflow, which models technical noise while preserving biological variation. Dimensionality reduction was carried out with PCA, and the top 30 components were used to compute a shared nearest neighbor (SNN) graph for clustering using the Leiden algorithm. UMAP was used for visualization. Following initial clustering, further manual filtering was applied to remove remaining doublets and low-quality subclusters. Specifically, subclusters containing >50% cells with low UMI counts or high doublet scores were excluded.

Cell Type Annotation via Label Transfer

Cell type annotation was performed using label transfer from a reference dataset generated by the Allen Brain Institute (10X V3)[23]. A subsampled version of this dataset, retaining 500 cells per cluster, was used as a reference. Subclass labels were transferred using Seurat's label transfer framework with rpca. Labels were transferred for gabaergic, glutamatergic, and non-neuronal cell types separately. Each subcluster of our scRNA-seq data was assigned a label if more than 80% of the cells within that subcluster were consistently mapped to a single reference label. For ambiguous clusters where label transfer results were inconsistent, manual annotation was performed using marker gene expression profiles to ensure accurate classification. This approach resulted in the identification of 80 distinct cell types in the snRNA-seq dataset. Given that the data was 10X multiome, these annotations were also available for the corresponding ATAC-seq data. We extended the labels to the male scATAC-seq data via our joint clustering of the data. Subclusters were assigned labels based on whether the majority of labelled nuclei —previously labeled through RNA-based annotation—mapped to a specific cell type. This ensured consistency in cell type annotation across both RNA and ATAC datasets.

MERFISH Gene Panel Design

To investigate cell-type-specific and age-associated transcriptional changes in the mouse brain, we designed a customized MERFISH panel consisting of 500 genes. Gene selection was informed by single-cell and spatial transcriptomic datasets, focusing on both cellular identity and biological processes implicated in aging. The panel includes 328 genes selected as cell type markers, capturing major neuronal and glial subtypes across brain regions. Marker genes were derived from comprehensive single-cell RNA-seq atlases[19,66] and a MERFISH-based spatial

atlas of the aging mouse brain[16]. From the latter, we prioritized genes with the highest variance across cells to ensure inclusion of the most informative spatial markers. To increase resolution for early neurogenic populations, we also included a focused subset of genes enriched in neural progenitor populations, such as radial glia-like cells and dentate gyrus progenitors. The remaining 172 genes were selected for their relevance to aging biology. These include genes differentially expressed with age in previous datasets, as well as genes involved in pathways such as chromatin remodeling, inflammation, oxidative stress, and circadian regulation. A subset of 24 genes was included based on prior evidence linking clock dysfunction to aging phenotypes[67]. MERFISH panel genes and their corresponding sources can be found in Table S2.

MERFISH tissue preparation and imaging

Brain slabs were embedded in OCT, rapidly frozen in isopentane and dry ice, and stored at −80 °C until ready for slicing. Coronal sections (12 µm thick) were collected from OCT-embedded tissue using a Leica CM1950 cryostat at −20 °C. Sections were immediately fixed in 4% paraformaldehyde (pre-warmed to 37 °C) for 30 minutes, then permeabilized in 70% ethanol according to the manufacturer's instructions. Sample preparation, including probe hybridization and gel embedding, was performed using the Vizgen sample preparation kit (10400012) following the provided protocol. Imaging was conducted with a MERSCOPE 500 Gene Imaging kit (Vizgen, 10400006) on a MERSCOPE system (Vizgen).

MERFISH data preprocessing

Following the data processing performed by the Vizgen MERSCOPE, the MERFISH data was first re-segmented using CellPose[68] (v2.1.1). Using the segmentation pipeline defined by the CellSegmentation class of the mftools package, the CellPose'cyto-2' model was used to perform a 2D segmentation on the 3rd z-slice of the DAPI stain images. These new segmentation masks were then used to regenerate the cell by gene matrix for downstream analysis. The MERFISH datasets were initially filtered to remove cells with less than 5 genes detected and to remove genes found in less than 3 cells. The datasets across all age groups were concatenated and processed using common Scanpy[69] (v1.10.0) functions in Python (v3.10.14). The datasets were first normalized to have the same total transcripts per cell and then log scaled, followed by principal component analysis (PCA). The nearest neighbors distance matrix was calculated with n_neighbors=30, then leiden clustering, PAGA, and UMAP were performed with default parameters. The combined object with 2 month, 9 month, and 18 month samples was then batch corrected using Scanpy's ComBat function. To perform a preliminary annotation of the processed MERFISH samples, the Allen Brain Cell Atlas 10Xv3 single-cell mouse brain dataset was used as a reference dataset[23]. The subclass level annotation was applied to the single-cell reference data, and this label was then transferred to the MERFISH data using the label_clusters function from the mftools package. The label_clusters function identifies the common genes between the MERFISH and reference data, then computes the mean z-scored expression of each cluster in the MERFISH and reference single-cell datasets. To transfer labels from the reference data to MERFISH, the Pearson correlation is computed between each MERFISH and reference cluster's expression profile, then the MERFISH cluster is assigned the

label of its most correlated single-cell reference cluster. This resulted in 34 different cell type labels that were transferred to the MERFISH dataset as an initial set of annotations.

Label transfer between snRNA and MERFISH for annotation

To assign cell type annotations to our MERFISH single-cell transcriptomic data, we performed label transfer from a matched snRNA-seq dataset using Seurat. We first subsampled the snRNA-seq reference to reduce the overrepresentation of large clusters, capping the maximum number of cells per annotated cluster at 2,000. Both the snRNA-seq and MERFISH datasets were normalized using SCTransform, and transfer anchors were computed using canonical correlation analysis (CCA) with the top 45 dimensions and all available genes (FindTransferAnchors, reduction = "cca"). Labels from the RNA-seq data (celltype_final) were transferred using TransferData, generating a predicted label and a confidence score (prediction.score.max) for each MERFISH cell. To mitigate potential noise and improve robustness, we refined the transferred labels through subclustering. Each MERFISH cluster sub-clustered at higher resolution (FindClusters, resolution = 2) following PCA-based preprocessing. For each resulting subcluster, we determined the majority predicted label based on cells with high confidence (score > 0.85). Any ambiguous subclusters were removed. For both modalities, gene expression was aggregated across cells of the same cell type using Seurat's AggregateExpression() function with centered log-ratio (CLR) normalization. The CLR transformation was applied per cell to adjust for differences in sequencing depth and compositional effects. For the RNA-seq data, gene expression values were further normalized by gene length to account for transcript length bias, yielding RPKM-like units based on CLR-normalized counts. Pearson correlation was computed across shared genes and cell types between the RNA-seq and MERFISH aggregated matrices. The resulting gene-by-gene correlation matrix was visualized as a heatmap to assess concordance in gene expression patterns across modalities (Figure S7).

Differential Gene Expression Analysis

Differential gene expression analysis was conducted using MAST[26], incorporating latent variables to account for percent mitochondrial reads, percent ribosomal reads, replicate, and brain region where necessary. Statistical significance was determined using likelihood ratio tests, and multiple comparisons were adjusted using the Benjamini-Hochberg correction. Genes were considered differentially expressed if they met a log2 fold-change of 0.25 and an adjusted p-value < 0.01.

Pathway Enrichment Analysis

Pathway enrichment analysis was performed using clusterProfiler[70] on significantly upregulated and downregulated genes with all genes used in the DEG analysis as background (genes expressed in > 1% of cells).

Peak Calling and Differential Accessibility Analysis

Peak calling and differential accessibility analysis were performed using SnapATAC2[20]. For peak calling, MACS3 was run on individual cell types using the snap.tl.macs3 function. Peaks were called separately for each cell type and age group using a q-value threshold of 0.01, with additional filtering against the ENCODE mm10 blacklist. To ensure robust peak detection, replicate-specific peaks were discarded. To identify differentially accessible regions (DARs), comparisons were made between 2-month-old and 18-month-old nuclei within each cell type. Peaks were filtered to include only those detected in at least 1% of cells in either age group. Differential testing was performed using snap.tl.diff_test, with a minimum log2 fold change of 0.25 and a significance threshold of adjusted p-value < 0.01. Up- and downregulated peaks were extracted and saved as BED files for downstream analysis. For visualization, aggregated peak matrices were generated for each cell type, region, and age group, normalized to reads per million (RPM).

Motif Enrichment Analysis

Motif enrichment analysis was performed using HOMER (v 4.11)[71] for the age-differential peaks in each cell type, with non-differential peaks as the background and default parameters.

Overlap with histone marks

We used bedtools intersect -c to overlap all called peaks for each cell type with H3K9me3 data from ENCODE[46]. H3K9me3 data from the forebrain were re-aligned to mm10 genome using BWA[72] without mapping quality filter (in order not to lose any reads aligning to repetitive elements), and peaks were re-called using SICER[73] on both ChIP-seq and input libraries, as described in[17].

Linking Genes to cCREs via ABC score

To associate genes with putative regulatory elements, we employed the Activity-By-Contact (ABC) model, which integrates chromatin accessibility, histone modifications, and 3D chromatin interactions to predict enhancer-gene links. The ABC score was calculated following the framework described by Fulco et al.[36], using open chromatin peaks as candidate cis-regulatory elements (cCREs).

Gaussian Smoothing for Hotspot Identification

We used the R package smoother to perform Gaussian smoothing on the number of differentially accessible regions (DARs) ($p < 0.01$, $|\log2 \text{ fold change}| > 1$) within each 100 kb region of the genome. A smoothing window length of 20 bins (~2.1 Mb span) was applied to account for local clustering of accessibility changes. Regions of the genome with a high concentration of DARs within a short distance were assigned higher Gaussian smoothing scores, and hotspots were defined as bins with smoothing scores in the top 1%, corresponding to a threshold of 0.2.

Quantifying transposable elements (TEs) accessibility

scTE[74] version 1.0 was used to build a genome index for the alignment of reads to genes (gencode vM21) and TEs (rmsk mm10) using scTE_build. The scTE command was used to map reads from the BAM files to transposable element families, generating a cell by feature read count matrix. A pseudo-bulk count table fo TE subfamilies was generated by summing reads from cells of the same cell type, age and biological replicate for each feature. Age-differential TEs for each cell type were then identified by DeSeq2[75] between 18-month and 2-month datasets using the likelihood ratio test.

Quantifying transposable elements (TEs) expression

SoloTE[76] was used to count reads at TE elements and genes directly from the Cellranger output, generating a Seurat object that contained the gene and TE count matrix. A pseudo-bulk count table for both genes and TEs was generated by summing reads from cells of the same cell type, age and biological replicate for each feature. Age-differential genes and TEs for each cell type were then identified by DeSeq2[75] between 18-month and 2-month datasets using the likelihood ratio test.

Supplementary tables

Table S1. Brain Dissection Region Annotation
Table S2. MERFISH gene panel
Table S3. ATAC Metadata
Table S4. RNA Metadata
Table S5. MERFISH Metadata
Table S6. cCREs called by celltype table

References

1. Mattson, M.P., and Arumugam, T.V. (2018). Hallmarks of brain aging: Adaptive and pathological modification by metabolic states. Cell Metab. *27*, 1176–1199.

2. Almanzar, N., Antony, J., Baghel, A.S., Bakerman, I., Bansal, I., Barres, B.A., Beachy, P.A., Berdnik, D., Bilen, B., Brownfield, D., et al. (2020). A single-cell transcriptomic atlas characterizes ageing tissues in the mouse. Nature *583*, 590–595.

3. Jin, K., Yao, Z., van Velthoven, C.T.J., Kaplan, E.S., Glattfelder, K., Barlow, S.T., Boyer, G., Carey, D., Casper, T., Chakka, A.B., et al. (2025). Brain-wide cell-type-specific transcriptomic signatures of healthy ageing in mice. Nature *638*, 182–196.

4. Klemm, S.L., Shipony, Z., and Greenleaf, W.J. (2019). Chromatin accessibility and the regulatory epigenome. Nat. Rev. Genet. *20*, 207–220.

5. López-Otín, C., Blasco, M.A., Partridge, L., Serrano, M., and Kroemer, G. (2023). Hallmarks of aging: An expanding universe. Cell *186*, 243–278.

6. Wang, K., Liu, H., Hu, Q., Wang, L., Liu, J., Zheng, Z., Zhang, W., Ren, J., Zhu, F., and Liu, G.-H. (2022). Epigenetic regulation of aging: implications for interventions of aging and diseases. Signal Transduct. Target. Ther. *7*, 1–22.

7. Patrick, R., Naval-Sanchez, M., Deshpande, N., Huang, Y., Zhang, J., Chen, X., Yang, Y., Tiwari, K., Esmaeili, M., Tran, M., et al. (2024). The activity of early-life gene regulatory elements is hijacked in aging through pervasive AP-1-linked chromatin opening. Cell Metab. *36*, 1858–1881.e23.

8. Lu, Y., Brommer, B., Tian, X., Krishnan, A., Meer, M., Wang, C., Vera, D.L., Zeng, Q., Yu, D., Bonkowski, M.S., et al. (2020). Reprogramming to recover youthful epigenetic information and restore vision. Nature *588*, 124–129.

9. Roichman, A., Elhanati, S., Aon, M.A., Abramovich, I., Di Francesco, A., Shahar, Y., Avivi, M.Y., Shurgi, M., Rubinstein, A., Wiesner, Y., et al. (2021). Restoration of energy homeostasis by SIRT6 extends healthy lifespan. Nat. Commun. *12*, 3208.

10. Akter, R., Afrose, A., Rahman, M.R., Chowdhury, R., Nirzhor, S.S.R., Khan, R.I., and Kabir, M.T. (2021). A Comprehensive Analysis into the Therapeutic Application of Natural Products as SIRT6 Modulators in Alzheimer's Disease, Aging, Cancer, Inflammation, and Diabetes. Int. J. Mol. Sci. *22*, 4180.

11. Liu, B., Wang, Z., Zhang, L., Ghosh, S., Zheng, H., and Zhou, Z. (2013). Depleting the methyltransferase Suv39h1 improves DNA repair and extends lifespan in a progeria mouse model. Nat. Commun. *4*, 1868.

12. Garcez, M.L., de Carvalho, C.A., Mina, F., Bellettini-Santos, T., Schiavo, G.L., da Silva, S., Campos, A.C.B.F., Varela, R.B., Valvassori, S.S., Damiani, A.P., et al. (2018). Sodium butyrate improves memory and modulates the activity of histone deacetylases in aged rats after the administration of d-galactose. Exp. Gerontol. *113*, 209–217.

13. Balzano, T., del Rey, N.L.-G., Esteban-García, N., Reinares-Sebastián, A., Pineda-Pardo, J.A., Trigo-Damas, I., Obeso, J.A., and Blesa, J. (2024). Neurovascular and immune factors of vulnerability of substantia nigra dopaminergic neurons in non-human primates. NPJ Parkinsons Dis. *10*, 1–11.

14. Ozawa, K., Suchanek, G., Breitschopf, H., Br€ck, W., Budka, H., Jellinger, K., and Lassmann, H. (1994). Patterns of oligodendroglia pathology in multiple sclerosis. Brain *117*, 1311–1322.

15. Rao, Y.L., Ganaraja, B., Murlimanju, B.V., Joy, T., Krishnamurthy, A., and Agrawal, A. (2022). Hippocampus and its involvement in Alzheimer's disease: a review. 3 Biotech *12*, 55.

16. Allen, W.E., Blosser, T.R., Sullivan, Z.A., Dulac, C., and Zhuang, X. (2023). Molecular and spatial signatures of mouse brain aging at single-cell resolution. Cell *186*, 194–208.e18.

17. Zhang, Y., Amaral, M.L., Zhu, C., Grieco, S.F., Hou, X., Lin, L., Buchanan, J., Tong, L., Preissl, S., Xu, X., et al. (2022). Single-cell epigenome analysis reveals age-associated

decay of heterochromatin domains in excitatory neurons in the mouse brain. Cell Res. *32*, 1008–1021.

18. Jagust, W. (2013). Vulnerable Neural Systems and the Borderland of Brain Aging and Neurodegeneration. Neuron *77*, 219–234.

19. Li, Y.E., Preissl, S., Hou, X., Zhang, Z., Zhang, K., Qiu, Y., Poirion, O.B., Li, B., Chiou, J., Liu, H., et al. (2021). An atlas of gene regulatory elements in adult mouse cerebrum. Nature *598*, 129–136.

20. Zhang, K., Zemke, N.R., Armand, E.J., and Ren, B. (2024). A fast, scalable and versatile tool for analysis of single-cell omics data. Nat. Methods *21*, 217–227.

21. Korsunsky, I., Millard, N., Fan, J., Slowikowski, K., Zhang, F., Wei, K., Baglaenko, Y., Brenner, M., Loh, P.-R., and Raychaudhuri, S. (2019). Fast, sensitive and accurate integration of single-cell data with Harmony. Nat. Methods *16*, 1289–1296.

22. Hahn, O., Foltz, A.G., Atkins, M., Kedir, B., Moran-Losada, P., Guldner, I.H., Munson, C., Kern, F., Pálovics, R., Lu, N., et al. (2023). Atlas of the aging mouse brain reveals white matter as vulnerable foci. Cell *186*, 4117–4133.e22.

23. Yao, Z., van Velthoven, C.T.J., Kunst, M., Zhang, M., McMillen, D., Lee, C., Jung, W., Goldy, J., Abdelhak, A., Aitken, M., et al. (2023). A high-resolution transcriptomic and spatial atlas of cell types in the whole mouse brain. Nature *624*, 317–332.

24. Zhang, Y., Liu, T., Meyer, C.A., Eeckhoute, J., Johnson, D.S., Bernstein, B.E., Nusbaum, C., Myers, R.M., Brown, M., Li, W., et al. (2008). Model-based analysis of ChIP-Seq (MACS). Genome Biol. *9*, R137.

25. Zu, S., Li, Y.E., Wang, K., Armand, E.J., Mamde, S., Amaral, M.L., Wang, Y., Chu, A., Xie, Y., Miller, M., et al. (2023). Single-cell analysis of chromatin accessibility in the adult mouse brain. Nature *624*, 378–389.

26. Finak, G., McDavid, A., Yajima, M., Deng, J., Gersuk, V., Shalek, A.K., Slichter, C.K., Miller, H.W., McElrath, M.J., Prlic, M., et al. (2015). MAST: a flexible statistical framework for assessing transcriptional changes and characterizing heterogeneity in single-cell RNA sequencing data. Genome Biol. *16*, 278.

27. Peters, A. (2002). The effects of normal aging on myelin and nerve fibers: a review. J. Neurocytol. *31*, 581–593.

28. Sun, D., Luo, M., Jeong, M., Rodriguez, B., Xia, Z., Hannah, R., Wang, H., Le, T., Faull, K.F., Chen, R., et al. (2014). Epigenomic profiling of young and aged HSCs reveals concerted changes during aging that reinforce self-renewal. Cell Stem Cell *14*, 673–688.

29. Hsu, L.C.-L., Nam, S., Cui, Y., Chang, C.-P., Wang, C.-F., Kuo, H.-C., Touboul, J.D., and Chou, S.-J. (2015). Lhx2 regulates the timing of β-catenin-dependent cortical neurogenesis. Proc. Natl. Acad. Sci. U. S. A. *112*, 12199–12204.

30. Subramanian, L., Sarkar, A., Shetty, A.S., Muralidharan, B., Padmanabhan, H., Piper, M., Monuki, E.S., Bach, I., Gronostajski, R.M., Richards, L.J., et al. (2011). Transcription factor Lhx2 is necessary and sufficient to suppress astrogliogenesis and promote neurogenesis in

the developing hippocampus. Proc. Natl. Acad. Sci. U. S. A. *108*, E265–E274.

31. Hou, P.-S., Chuang, C.-Y., Kao, C.-F., Chou, S.-J., Stone, L., Ho, H.-N., Chien, C.-L., and Kuo, H.-C. (2013). LHX2 regulates the neural differentiation of human embryonic stem cells via transcriptional modulation of PAX6 and CER1. Nucleic Acids Res. *41*, 7753–7770.

32. Sheeler, C., Rosa, J.-G., Ferro, A., McAdams, B., Borgenheimer, E., and Cvetanovic, M. (2020). Glia in Neurodegeneration: The Housekeeper, the Defender and the Perpetrator. Int. J. Mol. Sci. *21*, 9188.

33. Stolt, C.C., Rehberg, S., Ader, M., Lommes, P., Riethmacher, D., Schachner, M., Bartsch, U., and Wegner, M. (2002). Terminal differentiation of myelin-forming oligodendrocytes depends on the transcription factor Sox10. Genes Dev. *16*, 165–170.

34. Hughes, A.N., and Appel, B. (2019). Oligodendrocytes express synaptic proteins that modulate myelin sheath formation. Nat. Commun. *10*, 4125.

35. Bijlard, M., de Jonge, J.C., Klunder, B., Nomden, A., Hoekstra, D., and Baron, W. (2016). MAL is a regulator of the recruitment of myelin protein PLP to membrane microdomains. PLoS One *11*, e0155317.

36. Fulco, C.P., Nasser, J., Jones, T.R., Munson, G., Bergman, D.T., Subramanian, V., Grossman, S.R., Anyoha, R., Doughty, B.R., Patwardhan, T.A., et al. (2019). Activity-by-contact model of enhancer–promoter regulation from thousands of CRISPR perturbations. Nat. Genet. *51*, 1664–1669.

37. Gong, Z., Bilgel, M., Kiely, M., Triebswetter, C., Ferrucci, L., Resnick, S.M., Spencer, R.G., and Bouhrara, M. (2023). Lower myelin content is associated with more rapid cognitive decline among cognitively unimpaired individuals. Alzheimers. Dement. *19*, 3098–3107.

38. Ibañez, S., Sengupta, N., Luebke, J.I., Wimmer, K., and Weaver, C.M. (2024). Myelin dystrophy in the aging prefrontal cortex leads to impaired signal transmission and working memory decline: a multiscale computational study. eLife *12*. https://doi.org/10.7554/eLife.90964.2.

39. Clarke, L.E., Liddelow, S.A., Chakraborty, C., Münch, A.E., Heiman, M., and Barres, B.A. (2018). Normal aging induces A1-like astrocyte reactivity. Proc. Natl. Acad. Sci. U. S. A. *115*. https://doi.org/10.1073/pnas.1800165115.

40. Li, X., Li, Y., Jin, Y., Zhang, Y., Wu, J., Xu, Z., Huang, Y., Cai, L., Gao, S., Liu, T., et al. (2023). Transcriptional and epigenetic decoding of the microglial aging process. Nat. Aging *3*, 1288–1311.

41. Kaya, T., Mattugini, N., Liu, L., Ji, H., Cantuti-Castelvetri, L., Wu, J., Schifferer, M., Groh, J., Martini, R., Besson-Girard, S., et al. (2022). CD8+ T cells induce interferon-responsive oligodendrocytes and microglia in white matter aging. Nat. Neurosci. *25*, 1446–1457.

42. Flavell, S.W., Cowan, C.W., Kim, T.-K., Greer, P.L., Lin, Y., Paradis, S., Griffith, E.C., Hu, L.S., Chen, C., and Greenberg, M.E. (2006). Activity-dependent regulation of MEF2 transcription factors suppresses excitatory synapse number. Science *311*, 1008–1012.

43. Choi, W., Choe, M.S., Kim, S.M., Kim, S.J., Lee, J., Lee, Y., Lee, S.-M., Dho, S.H., Lee, M.-

Y., and Kim, L.K. (2024). RFX4 is an intrinsic factor for neuronal differentiation through induction of proneural genes POU3F2 and NEUROD1. Cell. Mol. Life Sci. *81*, 99.

44. Flaherty, E., and Maniatis, T. (2020). The role of clustered protocadherins in neurodevelopment and neuropsychiatric diseases. Curr. Opin. Genet. Dev. *65*, 144–150.

45. Schroeder, S., Sakib, M.S., Krüger, D., Pena, T., Burkhardt, S., Schütz, A.-L., Sananbenesi, F., and Fischer, A. (2024). LncRNA 3222401L13Rik Is Up-regulated in Aging Astrocytes and Regulates Neuronal Support Function Through Interaction with Npas3. Preprint, https://doi.org/10.1101/2024.08.14.607966 https://doi.org/10.1101/2024.08.14.607966.

46. He, Y., Hariharan, M., Gorkin, D.U., Dickel, D.E., Luo, C., Castanon, R.G., Nery, J.R., Lee, A.Y., Zhao, Y., Huang, H., et al. (2020). Spatiotemporal DNA methylome dynamics of the developing mouse fetus. Nature *583*, 752–759.

47. Wolf, B.K., Zhao, Y., McCray, A., Hawk, W.H., Deary, L.T., Sugiarto, N.W., LaCroix, I.S., Gerber, S.A., Cheng, C., and Wang, X. (2023). Cooperation of chromatin remodeling SWI/SNF complex and pioneer factor AP-1 shapes 3D enhancer landscapes. Nat. Struct. Mol. Biol. *30*, 10–21.

48. Wen, X., Luo, Z., Zhao, W., Calandrelli, R., Nguyen, T.C., Wan, X., Charles Richard, J.L., and Zhong, S. (2024). Single-cell multiplex chromatin and RNA interactions in ageing human brain. Nature *628*, 648–656.

49. Hajdarovic, K.H., Yu, D., Hassell, L.-A., Evans, S.A., Packer, S., Neretti, N., and Webb, A.E. (2022). Single-cell analysis of the aging female mouse hypothalamus. Nat. Aging *2*, 662–678.

50. Abdulai-Saiku, S., Gupta, S., Wang, D., Marino, F., Moreno, A.J., Huang, Y., Srivastava, D., Panning, B., and Dubal, D.B. (2025). The maternal X chromosome affects cognition and brain ageing in female mice. Nature *638*, 152–159.

51. Harris, J.J., Jolivet, R., and Attwell, D. (2012). Synaptic Energy Use and Supply. Neuron *75*, 762–777.

52. Yang, J.-H., Hayano, M., Griffin, P., Amorim, J.A., Bonkowski, M.S., Apostolides, J.K., Blanchette, M., Munding, E.M., Bhakta, M., Salfati, E.L., et al. (2021). Loss of Epigenetic Information as a Cause of Mammalian Aging. SSRN Electron. J. https://doi.org/10.2139/ssrn.3951490.

53. Fass, D.M., Reis, S.A., Ghosh, B., Hennig, K.M., Joseph, N.F., Zhao, W.-N., Nieland, T.J.F., Guan, J.-S., Groves Kuhnle, C.E., Tang, W., et al. (2013). Crebinostat: A novel cognitive enhancer that inhibits histone deacetylase activity and modulates chromatin-mediated neuroplasticity. Neuropharmacology *64*, 81–96.

54. Fontán-Lozano, Á., Romero-Granados, R., Troncoso, J., Múnera, A., Delgado-García, J.M., and Carrión, Á.M. (2008). Histone deacetylase inhibitors improve learning consolidation in young and in KA-induced-neurodegeneration and SAMP-8-mutant mice. Mol. Cell. Neurosci. *39*, 193–201.

55. Koche, R.P., Smith, Z.D., Adli, M., Gu, H., Ku, M., Gnirke, A., Bernstein, B.E., and

Meissner, A. (2011). Reprogramming Factor Expression Initiates Widespread Targeted Chromatin Remodeling. Cell Stem Cell *8*, 96–105.

56. Liu, H., Zeng, Q., Zhou, J., Bartlett, A., Wang, B.-A., Berube, P., Tian, W., Kenworthy, M., Altshul, J., Nery, J.R., et al. (2023). Single-cell DNA methylome and 3D multi-omic atlas of the adult mouse brain. Nature *624*, 366–377.

57. Wang, A., Chiou, J., Poirion, O.B., Buchanan, J., Valdez, M.J., Verheyden, J.M., Hou, X., Kudtarkar, P., Narendra, S., Newsome, J.M., et al. (2020). Single-cell multiomic profiling of human lungs reveals cell-type-specific and age-dynamic control of SARS-CoV2 host genes. Elife *9*, e62522.

58. Hocker, J.D., Poirion, O.B., Zhu, F., Buchanan, J., Zhang, K., Chiou, J., Wang, T.-M., Zhang, Q., Hou, X., Li, Y.E., et al. (2021). Cardiac cell type–specific gene regulatory programs and disease risk association. Sci. Adv. *7*, eabf1444.

59. Preissl, S., Fang, R., Huang, H., Zhao, Y., Raviram, R., Gorkin, D.U., Zhang, Y., Sos, B.C., Afzal, V., Dickel, D.E., et al. (2018). Single-nucleus analysis of accessible chromatin in developing mouse forebrain reveals cell-type-specific transcriptional regulation. Nat. Neurosci. *21*, 432–439.

60. Fang, R., Preissl, S., Li, Y., Hou, X., Lucero, J., Wang, X., Motamedi, A., Shiau, A.K., Zhou, X., Xie, F., et al. (2021). Comprehensive analysis of single cell ATAC-seq data with SnapATAC. Nat. Commun. *12*, 1337.

61. Zheng, G.X.Y., Terry, J.M., Belgrader, P., Ryvkin, P., Bent, Z.W., Wilson, R., Ziraldo, S.B., Wheeler, T.D., McDermott, G.P., Zhu, J., et al. (2017). Massively parallel digital transcriptional profiling of single cells. Nat. Commun. *8*, 14049.

62. Langmead, B., and Salzberg, S.L. (2012). Fast gapped-read alignment with Bowtie 2. Nat. Methods *9*, 357–359.

63. Wolock, S.L., Lopez, R., and Klein, A.M. (2019). Scrublet: Computational identification of cell Doublets in Single-cell transcriptomic data. Cell Syst. *8*, 281–291.e9.

64. ENCODE Project Consortium (2004). The ENCODE (ENCyclopedia Of DNA elements) Project. Science *306*, 636–640.

65. McGinnis, C.S., Murrow, L.M., and Gartner, Z.J. (2019). DoubletFinder: Doublet Detection in Single-Cell RNA Sequencing Data Using Artificial Nearest Neighbors. Cell Syst. *8*, 329–337.e4.

66. Zeisel, A., Hochgerner, H., Lönnerberg, P., Johnsson, A., Memic, F., van der Zwan, J., Häring, M., Braun, E., Borm, L.E., La Manno, G., et al. (2018). Molecular architecture of the mouse nervous system. Cell *174*, 999–1014.e22.

67. Buckley, M.T., Sun, E.D., George, B.M., Liu, L., Schaum, N., Xu, L., Reyes, J.M., Goodell, M.A., Weissman, I.L., Wyss-Coray, T., et al. (2023). Cell-type-specific aging clocks to quantify aging and rejuvenation in neurogenic regions of the brain. Nat. Aging *3*, 121–137.

68. Stringer, C., Wang, T., Michaelos, M., and Pachitariu, M. (2021). Cellpose: a generalist algorithm for cellular segmentation. Nat. Methods *18*, 100–106.

69. Wolf, F.A., Angerer, P., and Theis, F.J. (2018). SCANPY: large-scale single-cell gene expression data analysis. Genome Biol. *19*, 15.

70. Xu, S., Hu, E., Cai, Y., Xie, Z., Luo, X., Zhan, L., Tang, W., Wang, Q., Liu, B., Wang, R., et al. (2024). Using clusterProfiler to characterize multiomics data. Nat. Protoc. *19*, 3292–3320.

71. Heinz, S., Benner, C., Spann, N., Bertolino, E., Lin, Y.C., Laslo, P., Cheng, J.X., Murre, C., Singh, H., and Glass, C.K. (2010). Simple Combinations of Lineage-Determining Transcription Factors Prime \textitcis-Regulatory Elements Required for Macrophage and B Cell Identities. Mol. Cell *38*, 576–589.

72. Li, H., and Durbin, R. (2009). Fast and accurate short read alignment with Burrows–Wheeler transform. Bioinformatics *25*, 1754–1760.

73. Zang, C., Schones, D.E., Zeng, C., Cui, K., Zhao, K., and Peng, W. (2009). A clustering approach for identification of enriched domains from histone modification ChIP-Seq data. Bioinformatics *25*, 1952–1958.

74. He, J., Babarinde, I.A., Sun, L., Xu, S., Chen, R., Shi, J., Wei, Y., Li, Y., Ma, G., Zhuang, Q., et al. (2021). Identifying transposable element expression dynamics and heterogeneity during development at the single-cell level with a processing pipeline scTE. Nat. Commun. *12*, 1456.

75. Love, M.I., Huber, W., and Anders, S. (2014). Moderated estimation of fold change and dispersion for RNA-seq data with DESeq2. Genome Biol. *15*, 550.

76. Rodríguez-Quiroz, R., and Valdebenito-Maturana, B. (2022). SoloTE for improved analysis of transposable elements in single-cell RNA-Seq data using locus-specific expression. Commun. Biol. *5*, 1–12.

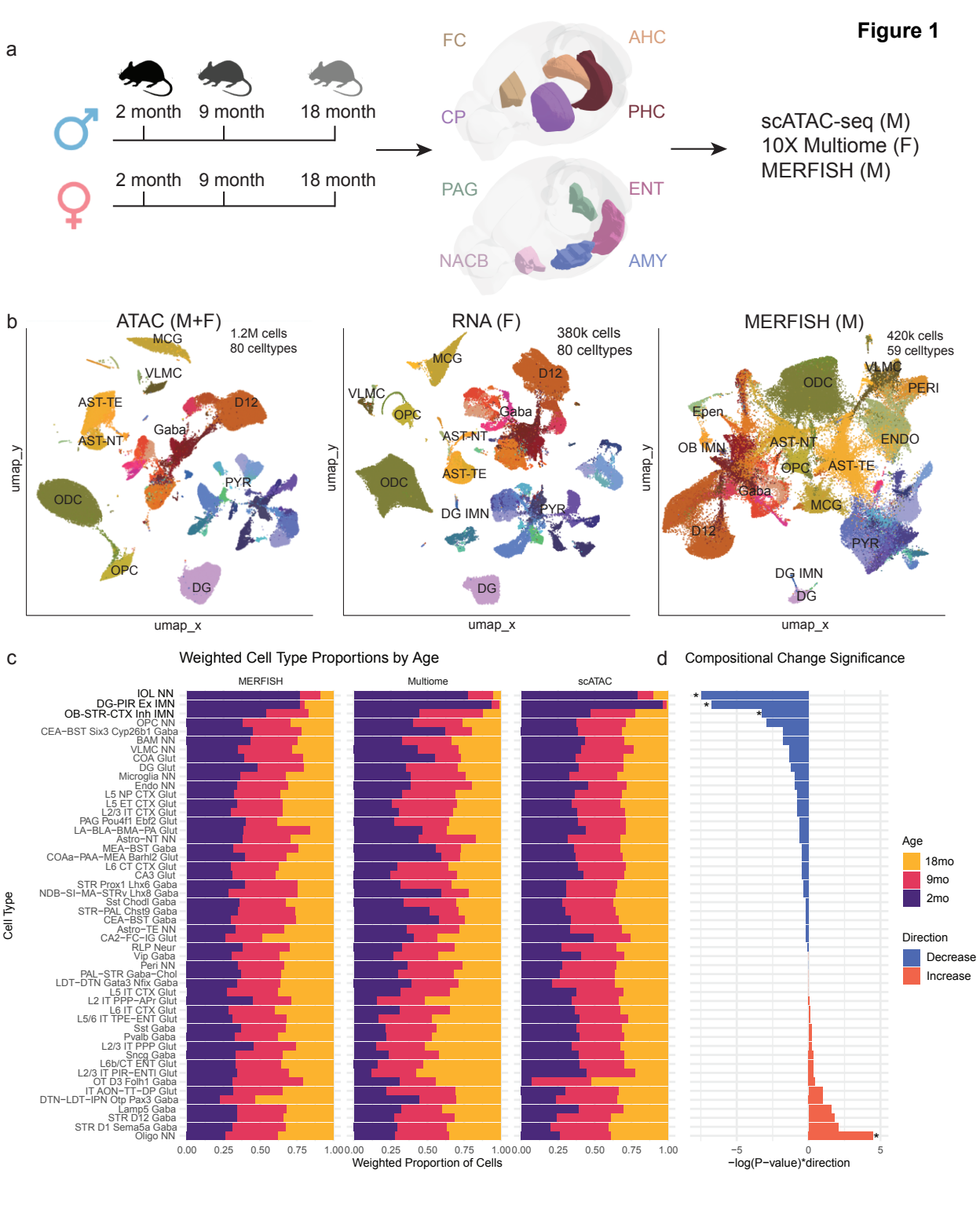
Figure 1
a
2 month
9 month
18 month
2 month
9 month
18 month
FC
AHC
CP
PHC
PAG
ENT
NACB
AMY
scATAC-seq (M)
10X Multiome (F)
MERFISH (M)
b
ATAC (M+F)
1.2M cells
80 celltypes
MCG
VLMC
AST-TE
D12
Gaba
AST-NT
PYR
ODC
OPC
DG
umap_y
umap_x
RNA (F)
380k cells
80 celltypes
MCG
D12
VLMC
OPC
Gaba
AST-NT
AST-TE
ODC
DG IMN
PYR
DG
umap_y
umap_x
MERFISH (M)
420k cells
59 celltypes
VLMC
ODC
PERI
Epen
OB IMN
AST-NT
ENDO
OPC
AST-TE
Gaba
MCG
D12
PYR
DG IMN
DG
umap_y
umap_x
c
Weighted Cell Type Proportions by Age
MERFISH
Multiome
scATAC
IOL NN
DG-PIR Ex IMN
OB-STR-CTX Inh IMN
OPC NN
CEA−BST Six3 Cyp26b1 Gaba
BAM NN
VLMC NN
COA Glut
DG Glut
Microglia NN
Endo NN
L5 NP CTX Glut
L5 ET CTX Glut
L2/3 IT CTX Glut
PAG Pou4f1 Ebf2 Glut
LA−BLA−BMA−PA Glut
Astro−NT NN
MEA−BST Gaba
COAa−PAA−MEA Barhl2 Glut
L6 CT CTX Glut
CA3 Glut
STR Prox1 Lhx6 Gaba
NDB−SI−MA−STRv Lhx8 Gaba
Sst Chodl Gaba
STR−PAL Chst9 Gaba
CEA−BST Gaba
Astro−TE NN
CA2−FC−IG Glut
RLP Neur
Vip Gaba
Peri NN
PAL−STR Gaba−Chol
LDT−DTN Gata3 Nfix Gaba
L5 IT CTX Glut
L2 IT PPP−APr Glut
L6 IT CTX Glut
L5/6 IT TPE−ENT Glut
Sst Gaba
Pvalb Gaba
L2/3 IT PPP Glut
Sncg Gaba
L6b/CT ENT Glut
L2/3 IT PIR−ENTl Glut
OT D3 Folh1 Gaba
IT AON−TT−DP Glut
DTN−LDT−IPN Otp Pax3 Gaba
Lamp5 Gaba
STR D12 Gaba
STR D1 Sema5a Gaba
Oligo NN
Cell Type
0.00
0.25
0.50
0.75
1.00
Weighted Proportion of Cells
d
Compositional Change Significance
−5
0
5
−log(P−value)*direction
Age
18mo
9mo
2mo
Direction
Decrease
Increase

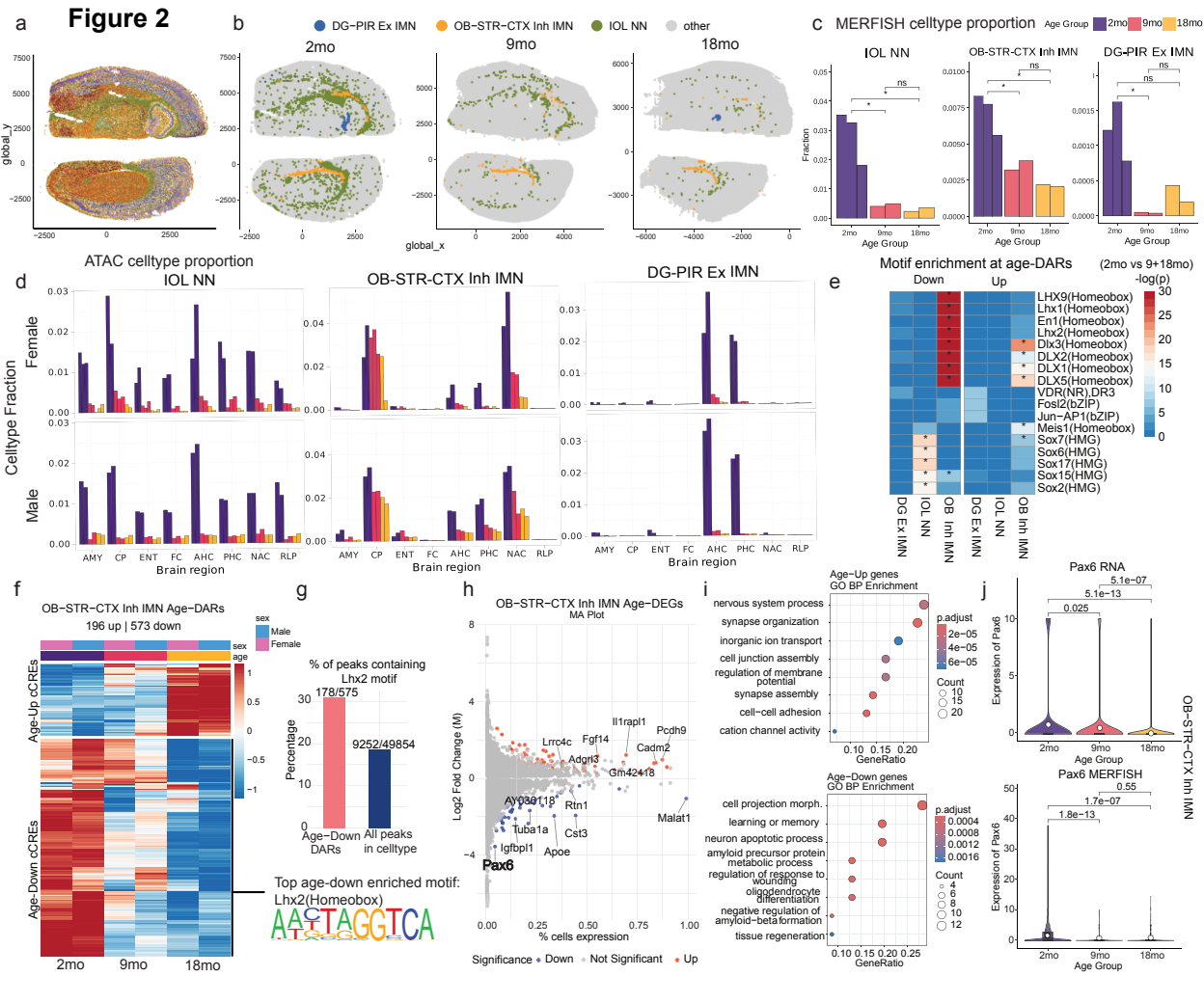
Figure 2
a
b
DG-PIR Ex IMN
OB-STR-CTX Inh IMN
IOL NN
other
2mo
9mo
18mo
global_y
global_x
c
MERFISH celltype proportion
Age Group
IOL NN
OB-STR-CTX Inh IMN
DG-PIR Ex IMN
Fraction
Age Group
d
ATAC celltype proportion
IOL NN
OB-STR-CTX Inh IMN
DG-PIR Ex IMN
Celltype Fraction
Female
Male
AMY
CP
ENT
FC
AHC
PHC
NAC
RLP
Brain region
e
Motif enrichment at age-DARs
(2mo vs 9+18mo)
-log(p)
Down
Up
LHX9(Homeobox)
Lhx1(Homeobox)
En1(Homeobox)
Lhx2(Homeobox)
Dlx3(Homeobox)
DLX2(Homeobox)
DLX1(Homeobox)
DLX5(Homeobox)
VDR(NR),DR3
Fosl2(bZIP)
Jun-AP1(bZIP)
Meis1(Homeobox)
Sox7(HMG)
Sox6(HMG)
Sox17(HMG)
Sox15(HMG)
Sox2(HMG)
DG Ex IMN
IOL NN
OB Inh IMN
f
OB-STR-CTX Inh IMN Age-DARs
196 up | 573 down
sex
Male
Female
age
Age-Up cCREs
Age-Down cCREs
2mo
9mo
18mo
g
% of peaks containing
Lhx2 motif
178/575
9252/49854
Percentage
Age-Down DARs
All peaks in celltype
Top age-down enriched motif:
Lhx2(Homeobox)
h
OB-STR-CTX Inh IMN Age-DEGs
MA Plot
Log2 Fold Change (M)
% cells expression
Il1rapl1
Pcdh9
Lrrc4c
Fgf14
Cadm2
Adgrl3
Gm42418
AY039118
Rtn1
Malat1
Tuba1a
Cst3
Igfbpl1
Apoe
Pax6
Significance
Down
Not Significant
Up
i
Age-Up genes
GO BP Enrichment
nervous system process
synapse organization
inorganic ion transport
cell junction assembly
regulation of membrane potential
synapse assembly
cell-cell adhesion
cation channel activity
p.adjust
Count
GeneRatio
Age-Down genes
GO BP Enrichment
cell projection morph.
learning or memory
neuron apoptotic process
amyloid precursor protein metabolic process
regulation of response to wounding
oligodendrocyte differentiation
negative regulation of amyloid-beta formation
tissue regeneration
j
Pax6 RNA
Pax6 MERFISH
Expression of Pax6
Age Group
OB-STR-CTX Inh IMN

Figure 3

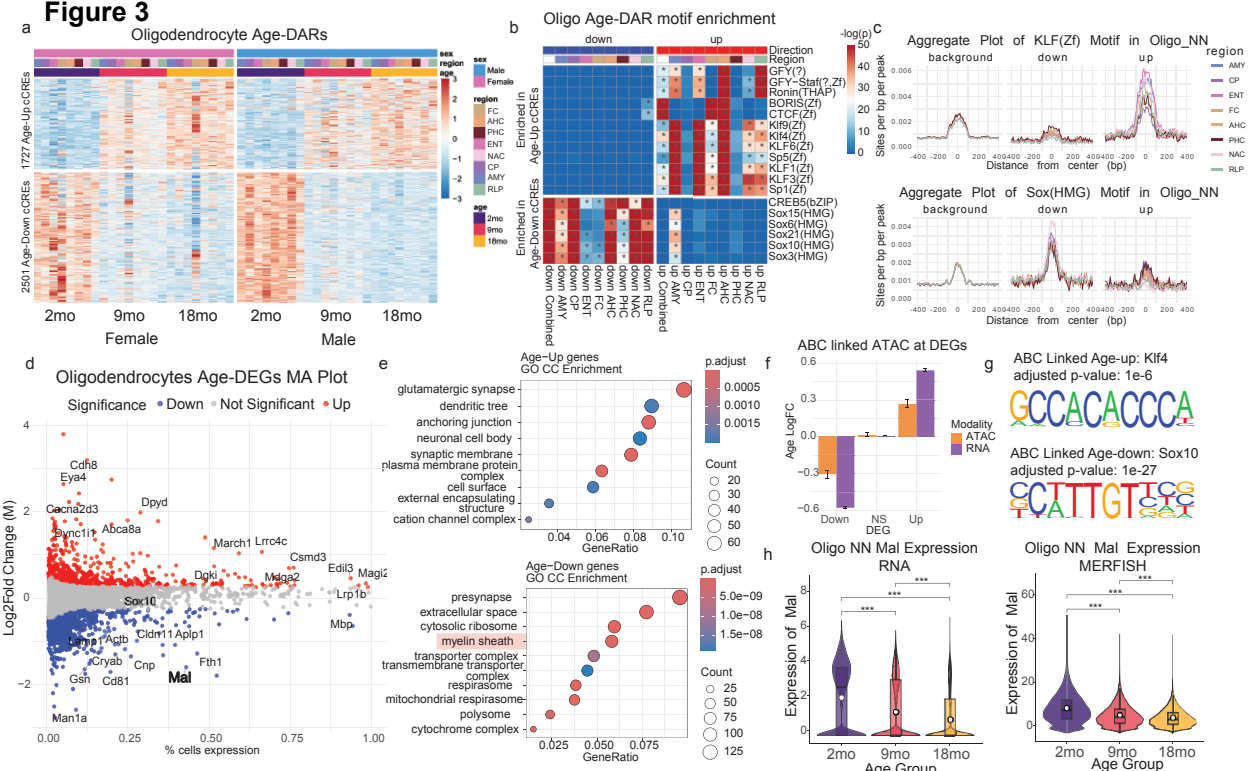
a
Oligodendrocyte Age-DARs
sex
region
age
Male
Female
FC
AHC
PHC
ENT
NAC
CP
AMY
RLP
2mo
9mo
18mo
1727 Age-Up cCREs
2501 Age-Down cCREs
2mo
9mo
18mo
Female
Male
b
Oligo Age-DAR motif enrichment
down
up
Direction
Region
GFY(?)
GFY~Staf(?_Zf)
Ronin(THAP)
BORIS(Zf)
CTCF(Zf)
Klf9(Zf)
Klf4(Zf)
KLF6(Zf)
Sp5(Zf)
KLF1(Zf)
KLF3(Zf)
Sp1(Zf)
CREB5(bZIP)
Sox15(HMG)
Sox6(HMG)
Sox21(HMG)
Sox10(HMG)
Sox3(HMG)
Enriched in Age-Up cCREs
Enriched in Age-Down cCREs
-log(p)
c
Aggregate Plot of KLF(Zf) Motif in Oligo_NN
background
down
up
Sites per bp per peak
Distance from center (bp)
region
AMY
CP
ENT
FC
AHC
PHC
NAC
RLP
Aggregate Plot of Sox(HMG) Motif in Oligo_NN
d
Oligodendrocytes Age-DEGs MA Plot
Significance
Down
Not Significant
Up
Cdh8
Eya4
Cacna2d3
Dpyd
Sync1
Abca8a
March1
Lrrc4
Csmd3
Edil3
Magi2
Dgki
Mdga2
Lrp1b
Sox10
Mbp
Hmgcr
Actb
Cldn11
Aplp1
Cryab
Cnp
Fth1
Gsn
Cd81
Mal
Man1a
Log2Fold Change (M)
% cells expression
e
Age−Up genes
GO CC Enrichment
glutamatergic synapse
dendritic tree
anchoring junction
neuronal cell body
synaptic membrane
plasma membrane protein complex
cell surface
external encapsulating structure
cation channel complex
GeneRatio
p.adjust
Count
Age−Down genes
GO CC Enrichment
presynapse
extracellular space
cytosolic ribosome
myelin sheath
transporter complex
transmembrane transporter complex
respirasome
mitochondrial respirasome
polysome
cytochrome complex
f
ABC linked ATAC at DEGs
Age LogFC
Modality
ATAC
RNA
Down
NS
Up
DEG
g
ABC Linked Age-up: Klf4
adjusted p-value: 1e-6
ABC Linked Age-down: Sox10
adjusted p-value: 1e-27
h
Oligo NN Mal Expression
RNA
Oligo NN Mal Expression
MERFISH
Expression of Mal
Age Group
2mo
9mo
18mo

Figure 4

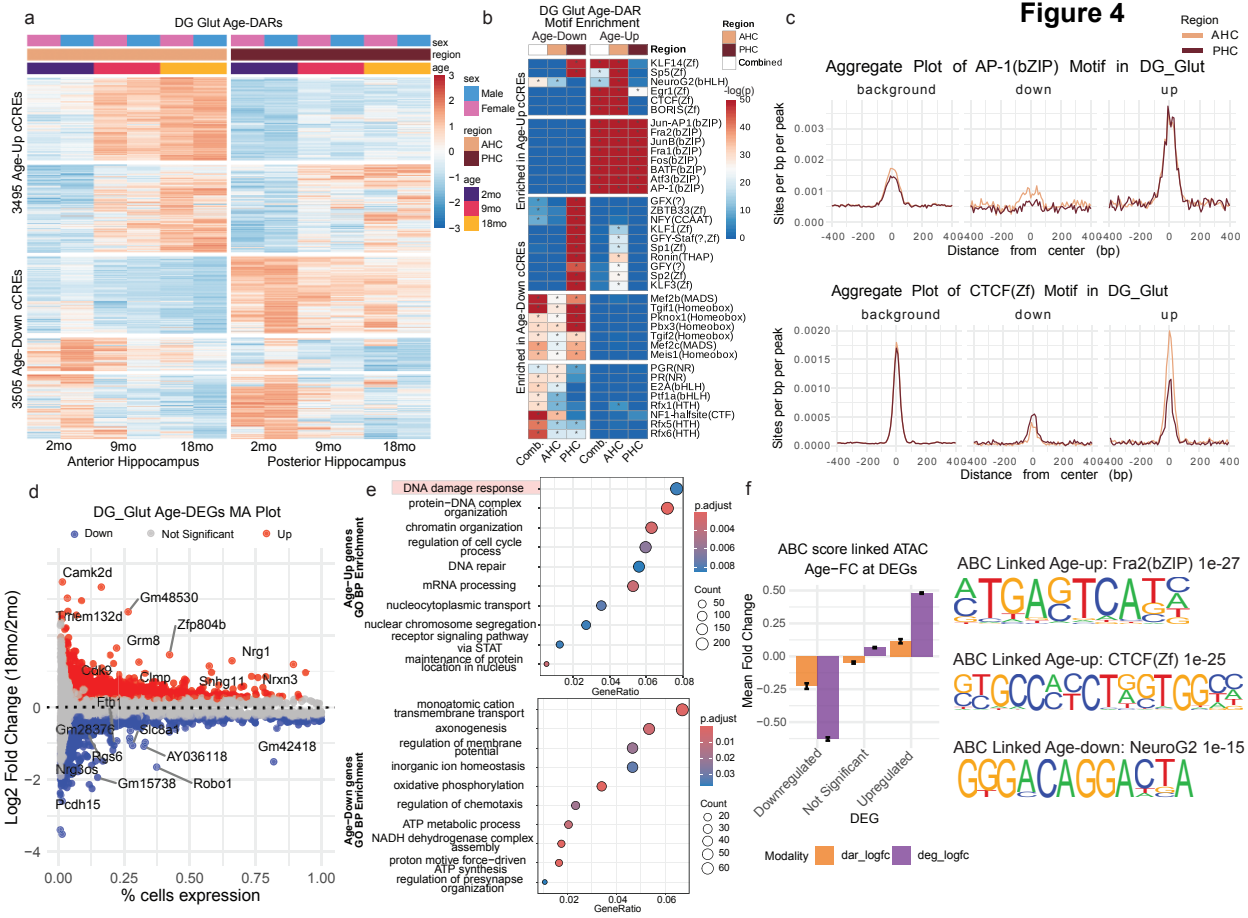
a
DG Glut Age-DARs
sex
region
age
Male
Female
AHC
PHC
2mo
9mo
18mo
3495 Age-Up cCREs
3505 Age-Down cCREs
Anterior Hippocampus
Posterior Hippocampus
b
DG Glut Age-DAR Motif Enrichment
Age-Down
Age-Up
Region
Combined
-log(p)
Enriched in Age-Up cCREs
Enriched in Age-Down cCREs
KLF14(Zf)
Sp5(Zf)
NeuroG2(bHLH)
Egr1(Zf)
CTCF(Zf)
BORIS(Zf)
Jun-AP1(bZIP)
Fra2(bZIP)
JunB(bZIP)
Fra1(bZIP)
Fos(bZIP)
BATF(bZIP)
Atf3(bZIP)
AP-1(bZIP)
GFX(?)
ZBTB33(Zf)
NFY(CCAAT)
KLF1(Zf)
GFY-Staf(?,Zf)
Sp1(Zf)
Ronin(THAP)
GFY(?)
Sp2(Zf)
KLF3(Zf)
Mef2b(MADS)
Tgif1(Homeobox)
Pknox1(Homeobox)
Pbx3(Homeobox)
Tgif2(Homeobox)
Mef2c(MADS)
Meis1(Homeobox)
PGR(NR)
PR(NR)
E2A(bHLH)
Ptf1a(bHLH)
Rfx1(HTH)
NF1-halfsite(CTF)
Rfx5(HTH)
Rfx6(HTH)
Comb.
AHC
PHC
c
Region
AHC
PHC
Aggregate Plot of AP-1(bZIP) Motif in DG_Glut
background
down
up
Sites per bp per peak
Distance from center (bp)
Aggregate Plot of CTCF(Zf) Motif in DG_Glut
d
DG_Glut Age-DEGs MA Plot
Down
Not Significant
Up
Camk2d
Gm48530
Trhem132d
Zfp804b
Grm8
Nrg1
Cdh9
Clmp
Snhg11
Nrxn3
Fbl
Gm28375
Slc8a1
Gm42418
Pgs6
AY036118
Nr3c2
Gm15738
Robo1
Pcdh15
Log2 Fold Change (18mo/2mo)
% cells expression
e
Age−Up genes GO BP Enrichment
DNA damage response
protein−DNA complex organization
chromatin organization
regulation of cell cycle process
DNA repair
mRNA processing
nucleocytoplasmic transport
nuclear chromosome segregation
receptor signaling pathway via STAT
maintenance of protein location in nucleus
p.adjust
Count
GeneRatio
Age−Down genes GO BP Enrichment
monoatomic cation transmembrane transport
axonogenesis
regulation of membrane potential
inorganic ion homeostasis
oxidative phosphorylation
regulation of chemotaxis
ATP metabolic process
NADH dehydrogenase complex assembly
proton motive force−driven ATP synthesis
regulation of presynapse organization
f
ABC score linked ATAC Age−FC at DEGs
Mean Fold Change
Downregulated
Not Significant
Upregulated
DEG
Modality
dar_logfc
deg_logfc
ABC Linked Age-up: Fra2(bZIP) 1e-27
ABC Linked Age-up: CTCF(Zf) 1e-25
ABC Linked Age-down: NeuroG2 1e-15

Figure 5

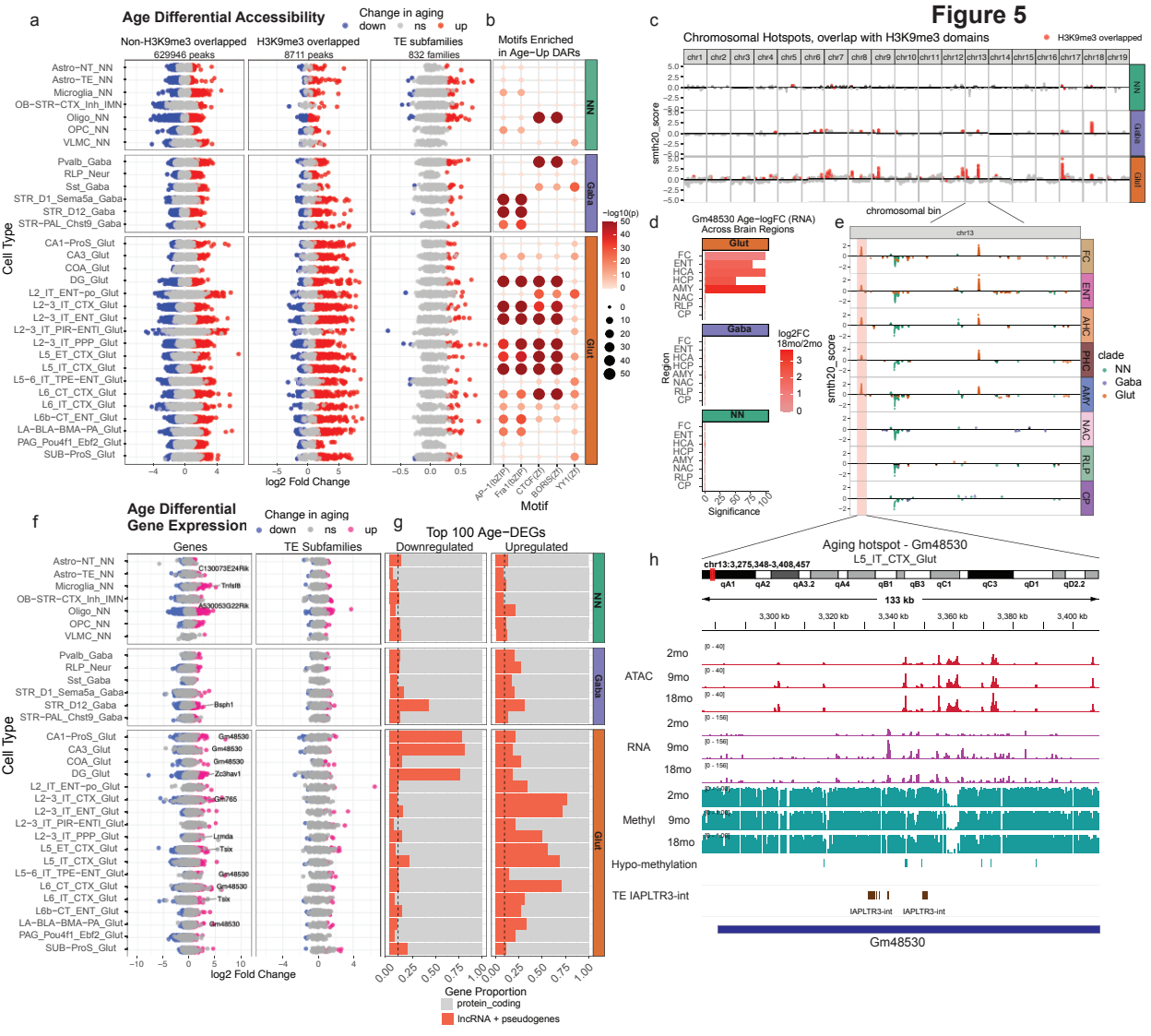
a
Age Differential Accessibility
Change in aging
down ns up
Non-H3K9me3 overlapped
629946 peaks
H3K9me3 overlapped
8711 peaks
TE subfamilies
832 families
Cell Type
log2 Fold Change
b
Motifs Enriched
in Age−Up DARs
Motif
−log10(p)
c
Chromosomal Hotspots, overlap with H3K9me3 domains
H3K9me3 overlapped
smth20_score
chromosomal bin
d
Gm48530 Age−logFC (RNA)
Across Brain Regions
Glut
Gaba
NN
Region
log2FC
18mo/2mo
Significance
e
chr13
smth20_score
clade
NN
Gaba
Glut
f
Age Differential
Gene Expression
Genes
TE Subfamilies
g
Top 100 Age−DEGs
Downregulated
Upregulated
Gene Proportion
protein_coding
lncRNA + pseudogenes
h
Aging hotspot - Gm48530
L5_IT_CTX_Glut
chr13:3,275,348-3,408,457
133 kb
ATAC
RNA
Methyl
Hypo-methylation
TE IAPLTR3-int
Gm48530

Figure S1

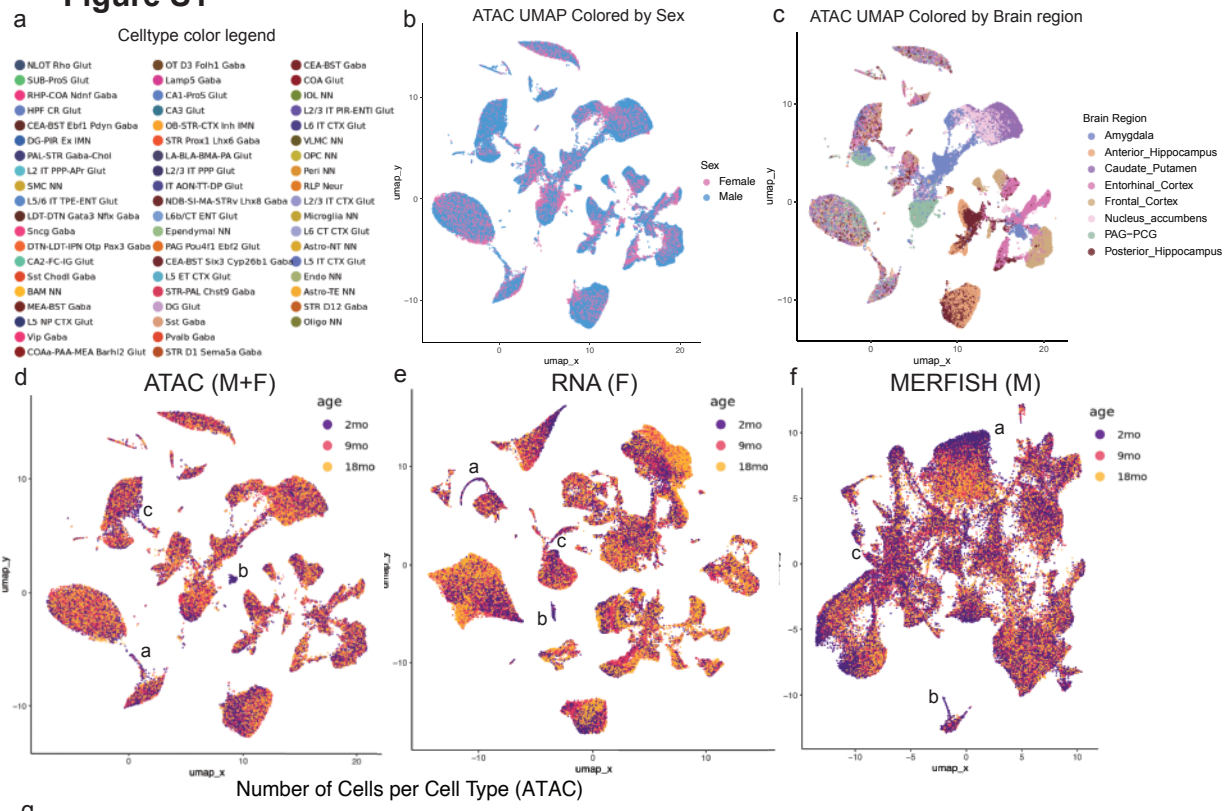
a
Celltype color legend
NLOT Rho Glut
SUB-ProS Glut
RHP-COA Ndnf Gaba
HPF CR Glut
CEA-BST Ebf1 Pdyn Gaba
DG-PIR Ex IMN
PAL-STR Gaba-Chol
L2 IT PPP-APr Glut
SMC NN
L5/6 IT TPE-ENT Glut
LDT-DTN Gata3 Nfix Gaba
Sncg Gaba
DTN-LDT-IPN Otp Pax3 Gaba
CA2-FC-IG Glut
Sst Chodl Gaba
BAM NN
MEA-BST Gaba
L5 NP CTX Glut
Vip Gaba
COAa-PAA-MEA Barhl2 Glut
OT D3 Folh1 Gaba
Lamp5 Gaba
CA1-ProS Glut
CA3 Glut
OB-STR-CTX Inh IMN
STR Prox1 Lhx6 Gaba
LA-BLA-BMA-PA Glut
L2/3 IT PPP Glut
IT AON-TT-DP Glut
NDB-SI-MA-STRv Lhx8 Gaba
L6b/CT ENT Glut
Ependymal NN
PAG Pou4f1 Ebf2 Glut
CEA-BST Six3 Cyp26b1 Gaba
L5 ET CTX Glut
STR-PAL Chst9 Gaba
DG Glut
Sst Gaba
Pvalb Gaba
STR D1 Sema5a Gaba
CEA-BST Gaba
COA Glut
IOL NN
L2/3 IT PIR-ENTl Glut
L6 IT CTX Glut
VLMC NN
OPC NN
Peri NN
RLP Neur
L2/3 IT CTX Glut
Microglia NN
L6 CT CTX Glut
Astro-NT NN
L5 IT CTX Glut
Endo NN
Astro-TE NN
STR D12 Gaba
Oligo NN
b
ATAC UMAP Colored by Sex
Sex
Female
Male
umap_y
umap_x
c
ATAC UMAP Colored by Brain region
Brain Region
Amygdala
Anterior_Hippocampus
Caudate_Putamen
Entorhinal_Cortex
Frontal_Cortex
Nucleus_accumbens
PAG-PCG
Posterior_Hippocampus
umap_y
umap_x
d
ATAC (M+F)
age
2mo
9mo
18mo
umap_y
umap_x
e
RNA (F)
age
2mo
9mo
18mo
umap_y
umap_x
f
MERFISH (M)
age
2mo
9mo
18mo
umap_x

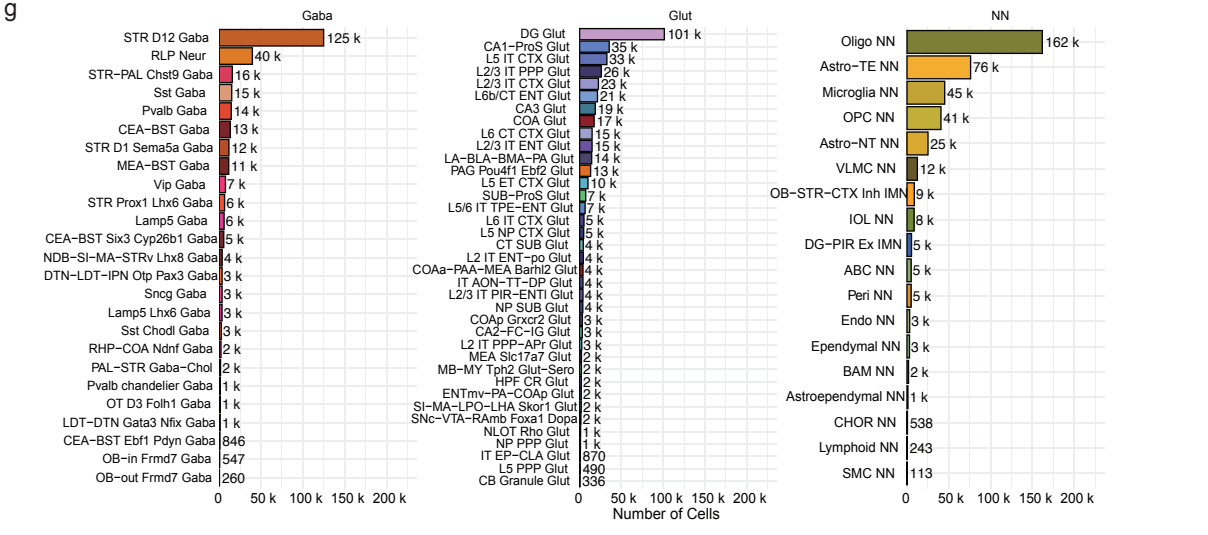
Number of Cells per Cell Type (ATAC)
g
Gaba
STR D12 Gaba 125 k
RLP Neur 40 k
STR-PAL Chst9 Gaba 16 k
Sst Gaba 15 k
Pvalb Gaba 14 k
CEA-BST Gaba 13 k
STR D1 Sema5a Gaba 12 k
MEA-BST Gaba 11 k
Vip Gaba 7 k
STR Prox1 Lhx6 Gaba 6 k
Lamp5 Gaba 6 k
CEA-BST Six3 Cyp26b1 Gaba 5 k
NDB-SI-MA-STRv Lhx8 Gaba 4 k
DTN-LDT-IPN Otp Pax3 Gaba 3 k
Sncg Gaba 3 k
Lamp5 Lhx6 Gaba 3 k
Sst Chodl Gaba 3 k
RHP-COA Ndnf Gaba 2 k
PAL-STR Gaba-Chol 2 k
Pvalb chandelier Gaba 1 k
OT D3 Folh1 Gaba 1 k
LDT-DTN Gata3 Nfix Gaba 1 k
CEA-BST Ebf1 Pdyn Gaba 846
OB-in Frmd7 Gaba 547
OB-out Frmd7 Gaba 260
0 50 k 100 k 150 k 200 k
Glut
DG Glut 101 k
CA1-ProS Glut 35 k
L5 IT CTX Glut 33 k
L2/3 IT PPP Glut 26 k
L2/3 IT CTX Glut 23 k
L6b/CT ENT Glut 21 k
CA3 Glut 19 k
COA Glut 17 k
L6 CT CTX Glut 15 k
L2/3 IT ENT Glut 15 k
LA-BLA-BMA-PA Glut 14 k
PAG Pou4f1 Ebf2 Glut 13 k
L5 ET CTX Glut 10 k
SUB-ProS Glut 7 k
L5/6 IT TPE-ENT Glut 7 k
L6 IT CTX Glut 5 k
L5 NP CTX Glut 5 k
CT SUB Glut 4 k
L2 IT ENT-po Glut 4 k
COAa-PAA-MEA Barhl2 Glut 4 k
IT AON-TT-DP Glut 4 k
L2/3 IT PIR-ENTl Glut 4 k
NP SUB Glut 4 k
COAp Grxcr2 Glut 3 k
CA2-FC-IG Glut 3 k
L2 IT PPP-APr Glut 3 k
MEA Slc17a7 Glut 2 k
MB-MY Tph2 Glut-Sero 2 k
HPF CR Glut 2 k
ENTmv-PA-COAp Glut 2 k
SI-MA-LPO-LHA Skor1 Glut 2 k
SNc-VTA-RAmb Foxa1 Dopa 2 k
NLOT Rho Glut 1 k
NP PPP Glut 1 k
IT EP-CLA Glut 870
L5 PPP Glut 490
CB Granule Glut 336
0 50 k 100 k 150 k 200 k
NN
Oligo NN 162 k
Astro-TE NN 76 k
Microglia NN 45 k
OPC NN 41 k
Astro-NT NN 25 k
VLMC NN 12 k
OB-STR-CTX Inh IMN 9 k
IOL NN 8 k
DG-PIR Ex IMN 5 k
ABC NN 5 k
Peri NN 5 k
Endo NN 3 k
Ependymal NN 3 k
BAM NN 2 k
Astroependymal NN 1 k
CHOR NN 538
Lymphoid NN 243
SMC NN 113
0 50 k 100 k 150 k 200 k
Number of Cells

Figure S2

a

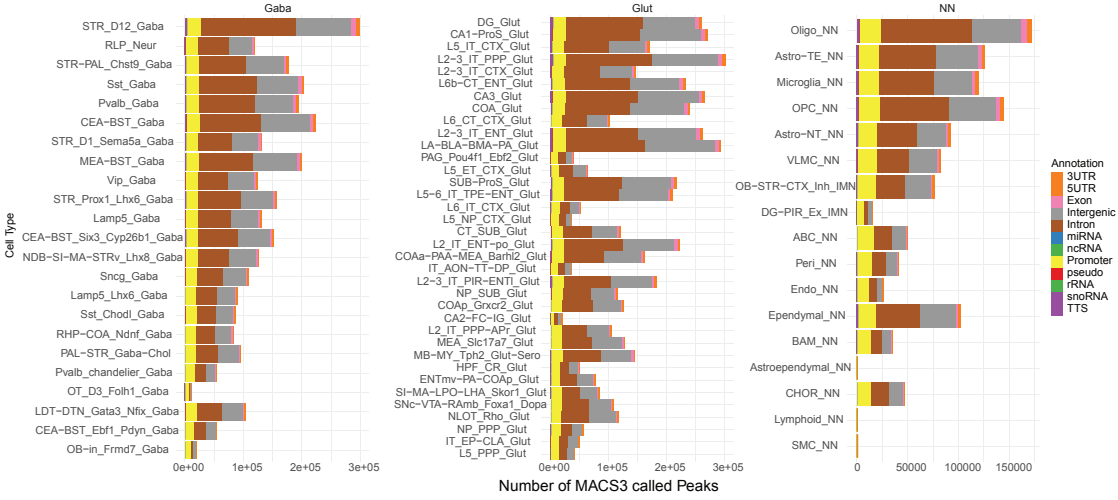
Called Peaks by Cell Type
Gaba
Glut
NN
Cell Type
STR_D12_Gaba
RLP_Neur
STR-PAL_Chst9_Gaba
Sst_Gaba
Pvalb_Gaba
CEA-BST_Gaba
STR_D1_Sema5a_Gaba
MEA-BST_Gaba
Vip_Gaba
STR_Prox1_Lhx6_Gaba
Lamp5_Gaba
CEA-BST_Six3_Cyp26b1_Gaba
NDB-SI-MA-STRv_Lhx8_Gaba
Sncg_Gaba
Lamp5_Lhx6_Gaba
Sst_Chodl_Gaba
RHP-COA_Ndnf_Gaba
PAL-STR_Gaba-Chol
Pvalb_chandelier_Gaba
OT_D3_Folh1_Gaba
LDT-DTN_Gata3_Nfix_Gaba
CEA-BST_Ebf1_Pdyn_Gaba
OB-in_Frmd7_Gaba
DG_Glut
CA1-ProS_Glut
L5_IT_CTX_Glut
L2-3_IT_PPP_Glut
L2-3_IT_CTX_Glut
L6b-CT_ENT_Glut
CA3_Glut
COA_Glut
L6_CT_CTX_Glut
L2-3_IT_ENT_Glut
LA-BLA-BMA-PA_Glut
PAG_Pou4f1_Ebf2_Glut
L5_ET_CTX_Glut
SUB-ProS_Glut
L5-6_IT_TPE-ENT_Glut
L6_IT_CTX_Glut
L5_NP_CTX_Glut
CT_SUB_Glut
L2_IT_ENT-po_Glut
COAa-PAA-MEA_Barhl2_Glut
IT_AON-TT-DP_Glut
L2-3_IT_PIR-ENTl_Glut
NP_SUB_Glut
COAp_Grxcr2_Glut
CA2-FC-IG_Glut
L2_IT_PPP-APr_Glut
MEA_Slc17a7_Glut
MB-MY_Tph2_Glut-Sero
HPF_CR_Glut
ENTmv-PA-COAp_Glut
SI-MA-LPO-LHA_Skor1_Glut
SNc-VTA-RAmb_Foxa1_Dopa
NLOT_Rho_Glut
NP_PPP_Glut
IT_EP-CLA_Glut
L5_PPP_Glut
Oligo_NN
Astro-TE_NN
Microglia_NN
OPC_NN
Astro-NT_NN
VLMC_NN
OB-STR-CTX_Inh_IMN
DG-PIR_Ex_IMN
ABC_NN
Peri_NN
Endo_NN
Ependymal_NN
BAM_NN
Astroependymal_NN
CHOR_NN
Lymphoid_NN
SMC_NN
0e+00
1e+05
2e+05
3e+05
0
50000
100000
150000
Number of MACS3 called Peaks
Annotation
3UTR
5UTR
Exon
Intergenic
Intron
miRNA
ncRNA
Promoter
pseudo
rRNA
snoRNA
TTS

b

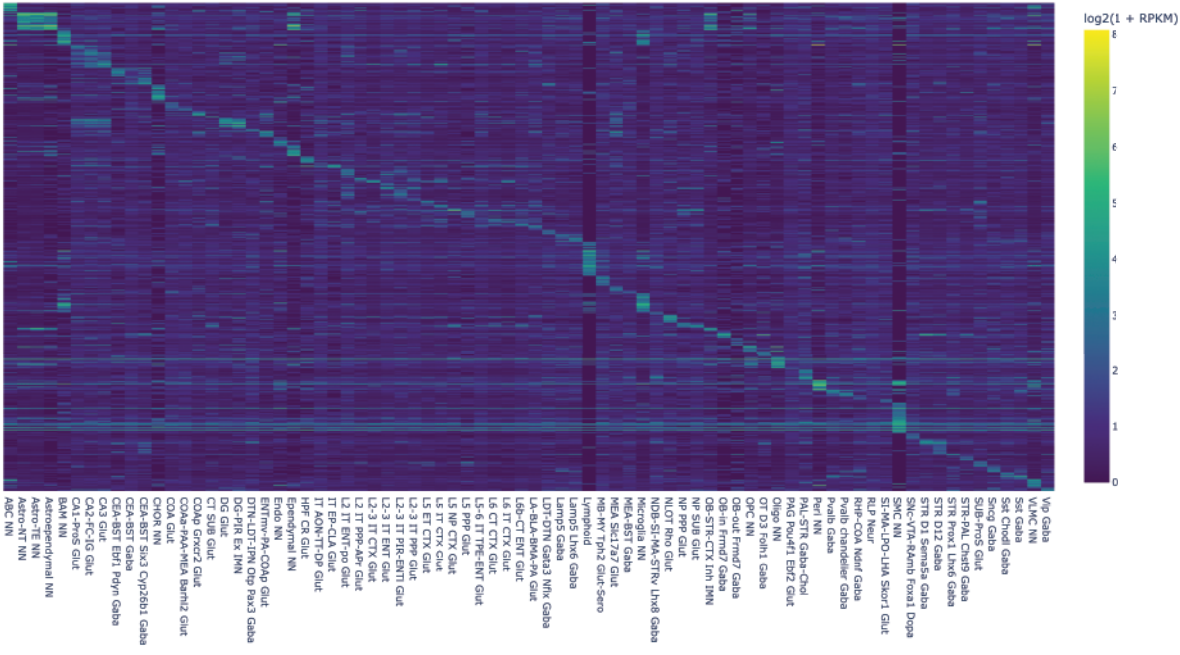
776,358 marker cCREs across celltypes
log2(1 + RPKM)
0
1
2
3
4
5
6
7
8
ABC NN
Astro-TE NN
Astro-NT NN
Astroependymal NN
BAM NN
CA1-ProS Glut
CA2-FC-IG Glut
CA3 Glut
CEA-BST Ebf1 Pdyn Gaba
CEA-BST Gaba
CEA-BST Six3 Cyp26b1 Gaba
CHOR NN
COA Glut
COAa-PAA-MEA Barhl2 Glut
COAp Grxcr2 Glut
CT SUB Glut
DG Glut
DG-PIR Ex IMN
DTN-LDT-LPN Otp Pax3 Gaba
Endo NN
ENTmv-PA-COAp Glut
Ependymal NN
HPF CR Glut
IT AON-TT-DP Glut
IT EP-CLA Glut
L2 IT ENT-po Glut
L2 IT PPP-APr Glut
L2-3 IT CTX Glut
L2-3 IT ENT Glut
L2-3 IT PIR-ENTl Glut
L2-3 IT PPP Glut
L5 ET CTX Glut
L5 IT CTX Glut
L5 NP CTX Glut
L5 PPP Glut
L5-6 IT TPE-ENT Glut
L6 CT CTX Glut
L6 IT CTX Glut
L6b-CT ENT Glut
LA-BLA-BMA-PA Glut
LDT-DTN Gata3 Nfix Gaba
Lamp5 Gaba
Lamp5 Lhx6 Gaba
Lymphoid
MB-MY Tph2 Glut-Sero
MEA Slc17a7 Glut
MEA-BST Gaba
Microglia NN
NDB-SI-MA-STRv Lhx8 Gaba
NLOT Rho Glut
NP PPP Glut
NP SUB Glut
OB-STR-CTX Inh IMN
OB-out Frmd7 Gaba
OPC NN
OT D3 Folh1 Gaba
Oligo NN
PAG Pou4f1 Ebf2 Glut
PAL-STR Gaba-Chol
Peri NN
Pvalb Gaba
Pvalb chandelier Gaba
RHP-COA Ndnf Gaba
RLP Neur
SI-MA-LPO-LHA Skor1 Glut
SMC NN
SNc-VTA-RAmb Foxa1 Dopa
STR D1 Sema5a Gaba
STR D12 Gaba
STR Prox1 Lhx6 Gaba
STR-PAL Chst9 Gaba
SUB-ProS Glut
Sncg Gaba
Sst Chodl Gaba
Sst Gaba
VLMC NN
Vip Gaba

Figure S3

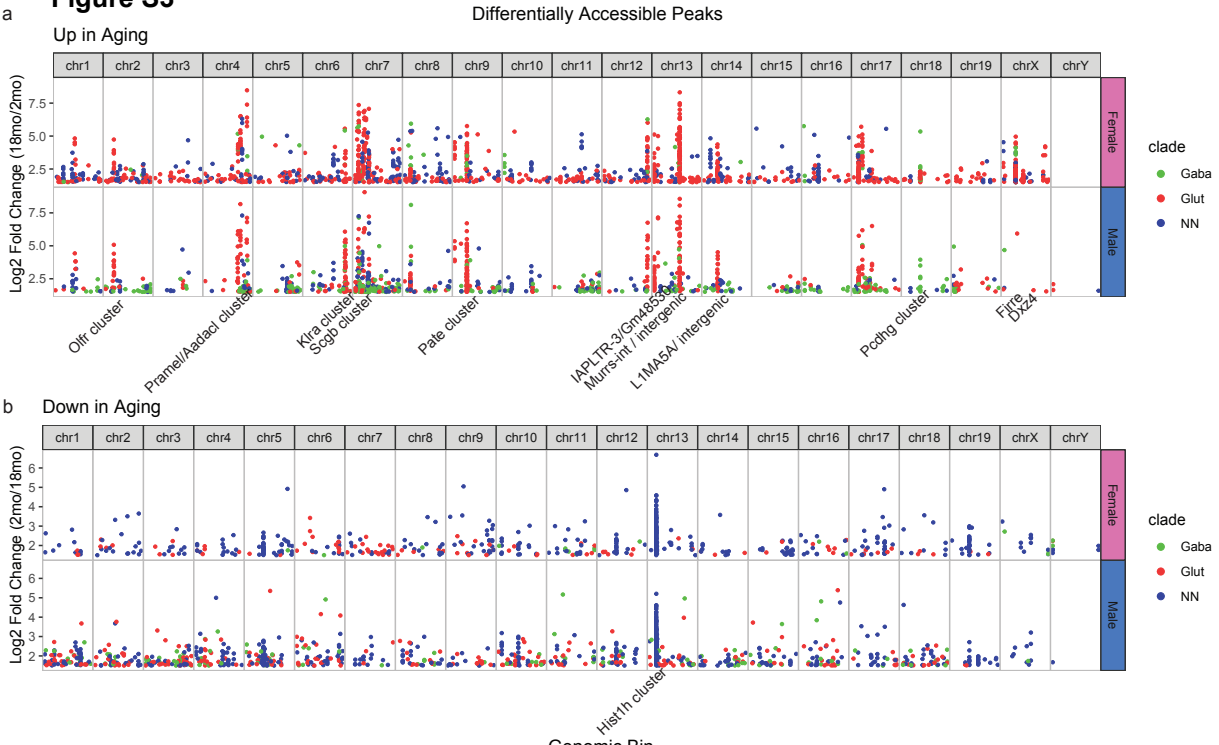
a
Differentially Accessible Peaks
Up in Aging
chr1
chr2
chr3
chr4
chr5
chr6
chr7
chr8
chr9
chr10
chr11
chr12
chr13
chr14
chr15
chr16
chr17
chr18
chr19
chrX
chrY
Log2 Fold Change (18mo/2mo)
7.5
5.0
2.5
Female
Male
clade
Gaba
Glut
NN
Olfr cluster
Pramel/Aadacl cluster
Klra cluster
Scgb cluster
Pate cluster
IAPLTR-3/Gm4853
Murrs-int / intergenic
L1MA5A/ intergenic
Pcdhg cluster
Firre
Dxz4
b
Down in Aging
Log2 Fold Change (2mo/18mo)
6
5
4
3
2
Hist1h cluster
Genomic Bin

Figure S4

a

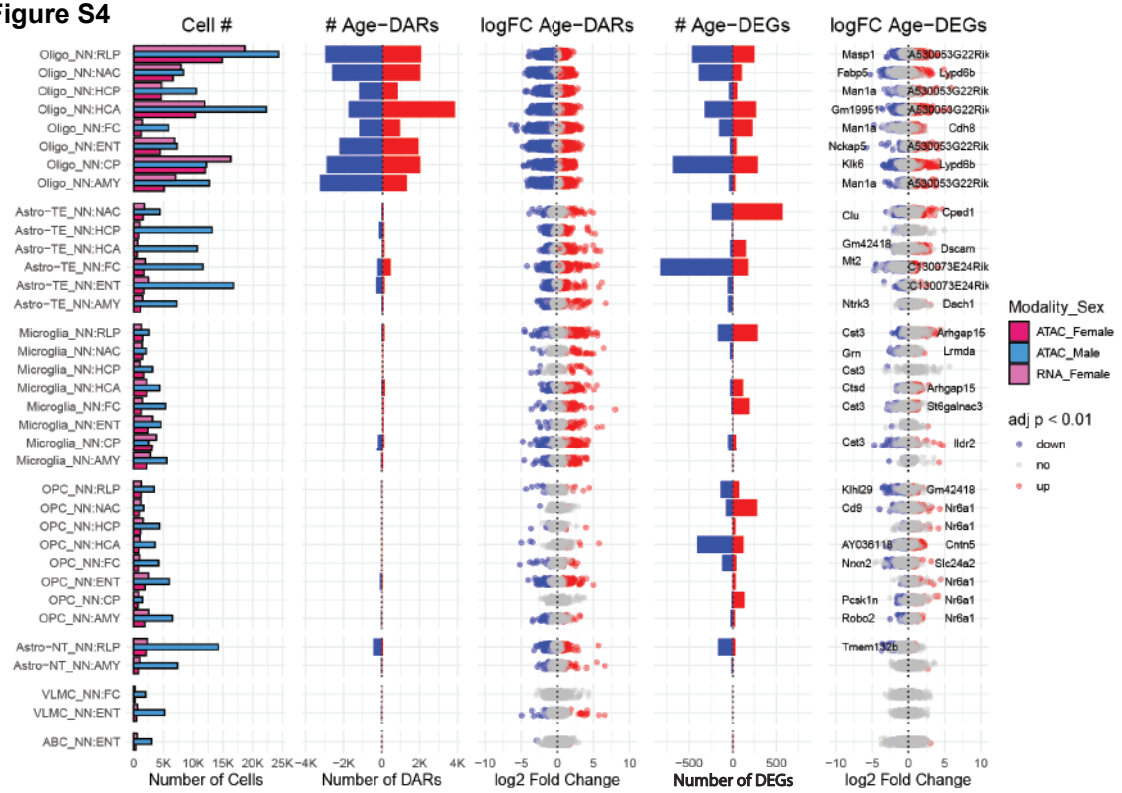
Cell #
Age−DARs
logFC Age−DARs
Age−DEGs
logFC Age−DEGs
Oligo_NN:RLP
Oligo_NN:NAC
Oligo_NN:HCP
Oligo_NN:HCA
Oligo_NN:FC
Oligo_NN:ENT
Oligo_NN:CP
Oligo_NN:AMY
Astro−TE_NN:NAC
Astro−TE_NN:HCP
Astro−TE_NN:HCA
Astro−TE_NN:FC
Astro−TE_NN:ENT
Astro−TE_NN:AMY
Microglia_NN:RLP
Microglia_NN:NAC
Microglia_NN:HCP
Microglia_NN:HCA
Microglia_NN:FC
Microglia_NN:ENT
Microglia_NN:CP
Microglia_NN:AMY
OPC_NN:RLP
OPC_NN:NAC
OPC_NN:HCP
OPC_NN:HCA
OPC_NN:FC
OPC_NN:ENT
OPC_NN:CP
OPC_NN:AMY
Astro−NT_NN:RLP
Astro−NT_NN:AMY
VLMC_NN:FC
VLMC_NN:ENT
ABC_NN:ENT
Number of Cells
Number of DARs
log2 Fold Change
Number of DEGs
log2 Fold Change
Modality_Sex
ATAC_Female
ATAC_Male
RNA_Female
adj p < 0.01
down
no
up

b

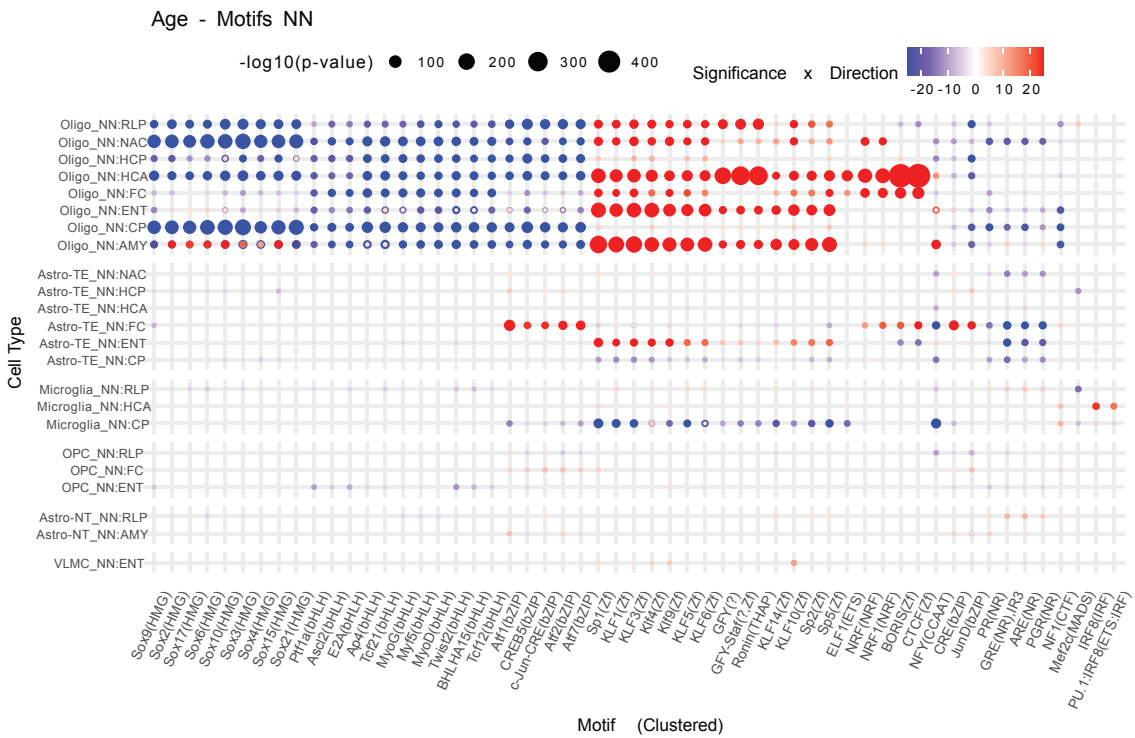
Age - Motifs NN
-log10(p-value)
100
200
300
400
Significance x Direction
-20 -10 0 10 20
Cell Type
Motif (Clustered)

Figure S5

a

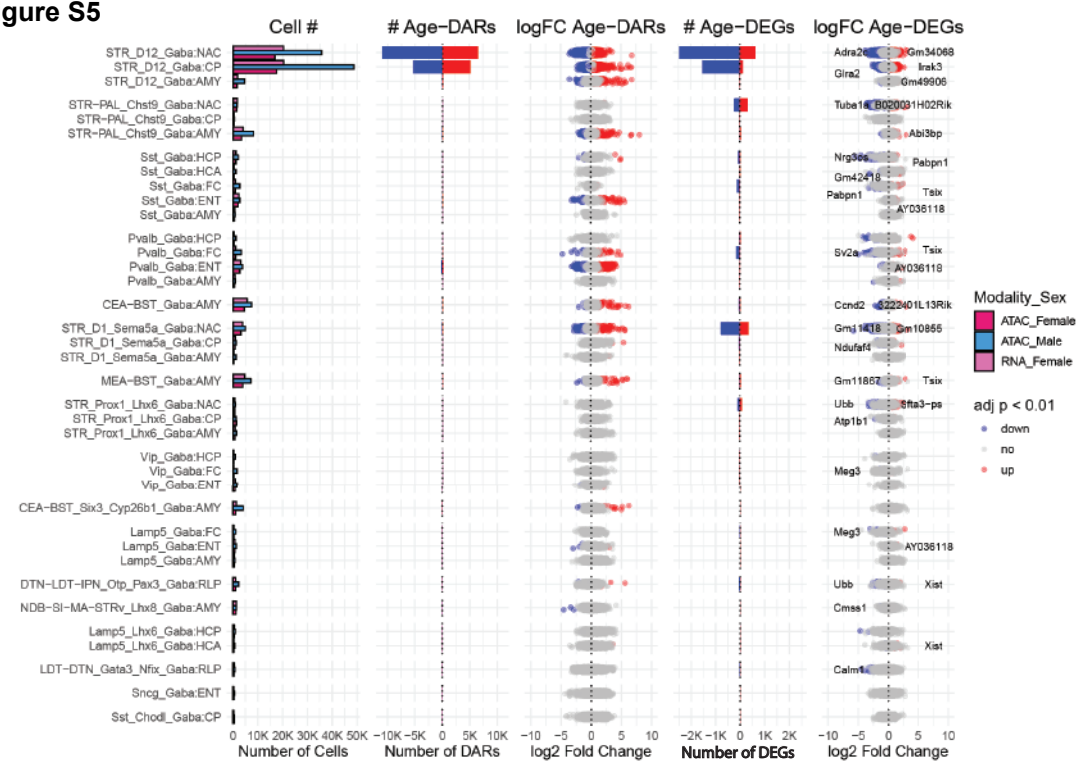
Cell #
Age−DARs
logFC Age−DARs
Age−DEGs
logFC Age−DEGs
STR_D12_Gaba:NAC
STR_D12_Gaba:CP
STR_D12_Gaba:AMY
STR−PAL_Chst9_Gaba:NAC
STR−PAL_Chst9_Gaba:CP
STR−PAL_Chst9_Gaba:AMY
Sst_Gaba:HCP
Sst_Gaba:HCA
Sst_Gaba:FC
Sst_Gaba:ENT
Sst_Gaba:AMY
Pvalb_Gaba:HCP
Pvalb_Gaba:FC
Pvalb_Gaba:ENT
Pvalb_Gaba:AMY
CEA−BST_Gaba:AMY
STR_D1_Sema5a_Gaba:NAC
STR_D1_Sema5a_Gaba:CP
STR_D1_Sema5a_Gaba:AMY
MEA−BST_Gaba:AMY
STR_Prox1_Lhx6_Gaba:NAC
STR_Prox1_Lhx6_Gaba:CP
STR_Prox1_Lhx6_Gaba:AMY
Vip_Gaba:HCP
Vip_Gaba:FC
Vip_Gaba:ENT
CEA−BST_Six3_Cyp26b1_Gaba:AMY
Lamp5_Gaba:FC
Lamp5_Gaba:ENT
Lamp5_Gaba:AMY
DTN−LDT−IPN_Otp_Pax3_Gaba:RLP
NDB−SI−MA−STRv_Lhx8_Gaba:AMY
Lamp5_Lhx6_Gaba:HCP
Lamp5_Lhx6_Gaba:HCA
LDT−DTN_Gata3_Nfix_Gaba:RLP
Sncg_Gaba:ENT
Sst_Chodl_Gaba:CP
Adra2c
Gm34068
Gira2
Irak3
Gm49906
Tuba1a
B020031H02Rik
Abi3bp
Nrg3os
Pabpn1
Gm42418
Tsix
AY036118
Sv2a
Ccnd2
6222401L13Rik
Gm11418
Gm10855
Ndufaf4
Gm11867
Ubb
Sfta3−ps
Atp1b1
Meg3
Xist
Cmss1
Calm1
Modality_Sex
ATAC_Female
ATAC_Male
RNA_Female
adj p < 0.01
down
no
up
Number of Cells
Number of DARs
log2 Fold Change
Number of DEGs
log2 Fold Change

b

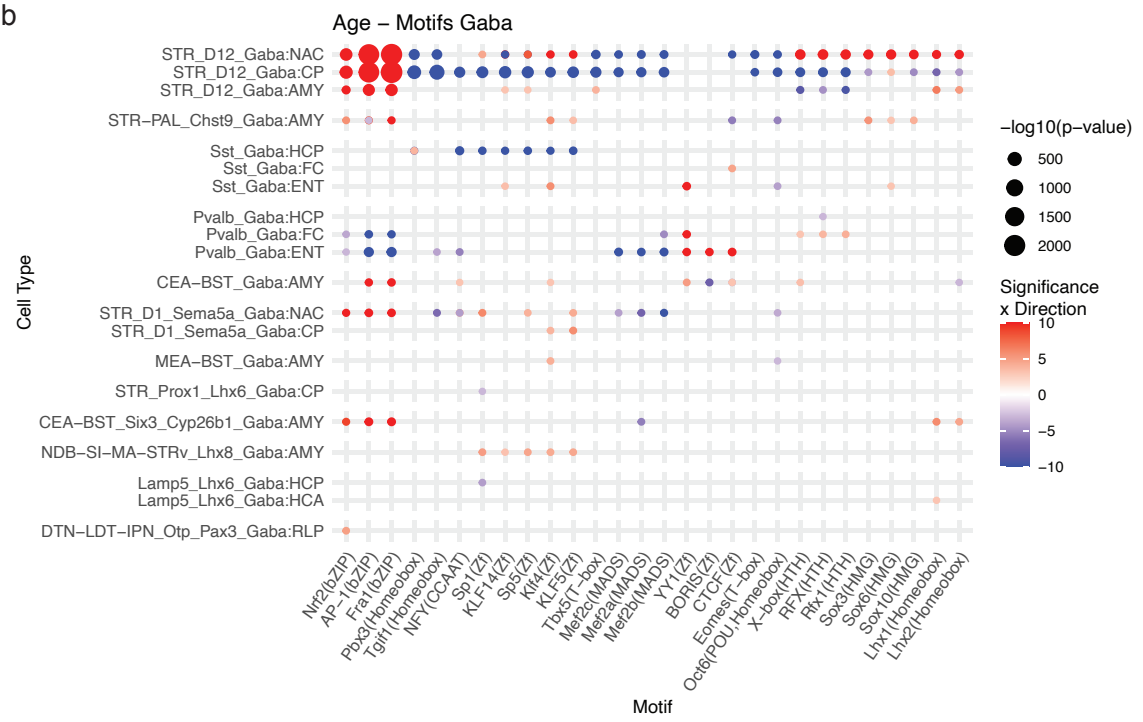
Age − Motifs Gaba
STR_D12_Gaba:NAC
STR_D12_Gaba:CP
STR_D12_Gaba:AMY
STR−PAL_Chst9_Gaba:AMY
Sst_Gaba:HCP
Sst_Gaba:FC
Sst_Gaba:ENT
Pvalb_Gaba:HCP
Pvalb_Gaba:FC
Pvalb_Gaba:ENT
CEA−BST_Gaba:AMY
STR_D1_Sema5a_Gaba:NAC
STR_D1_Sema5a_Gaba:CP
MEA−BST_Gaba:AMY
STR_Prox1_Lhx6_Gaba:CP
CEA−BST_Six3_Cyp26b1_Gaba:AMY
NDB−SI−MA−STRv_Lhx8_Gaba:AMY
Lamp5_Lhx6_Gaba:HCP
Lamp5_Lhx6_Gaba:HCA
DTN−LDT−IPN_Otp_Pax3_Gaba:RLP
Cell Type
Nrf2(bZIP)
AP−1(bZIP)
Fra1(bZIP)
Pbx3(Homeobox)
Tgif1(Homeobox)
NFY(CCAAT)
Sp1(Zf)
KLF14(Zf)
Sp5(Zf)
Klf4(Zf)
KLF5(Zf)
Tbx5(T−box)
Mef2c(MADS)
Mef2a(MADS)
Mef2b(MADS)
YY1(Zf)
BORIS(Zf)
CTCF(Zf)
Eomes(T−box)
Oct6(POU,Homeobox)
X−box(HTH)
RFX(HTH)
Rfx1(HTH)
Sox3(HMG)
Sox6(HMG)
Sox10(HMG)
Lhx1(Homeobox)
Lhx2(Homeobox)
Motif
−log10(p−value)
500
1000
1500
2000
Significance x Direction
10
5
0
−5
−10

Figure S6

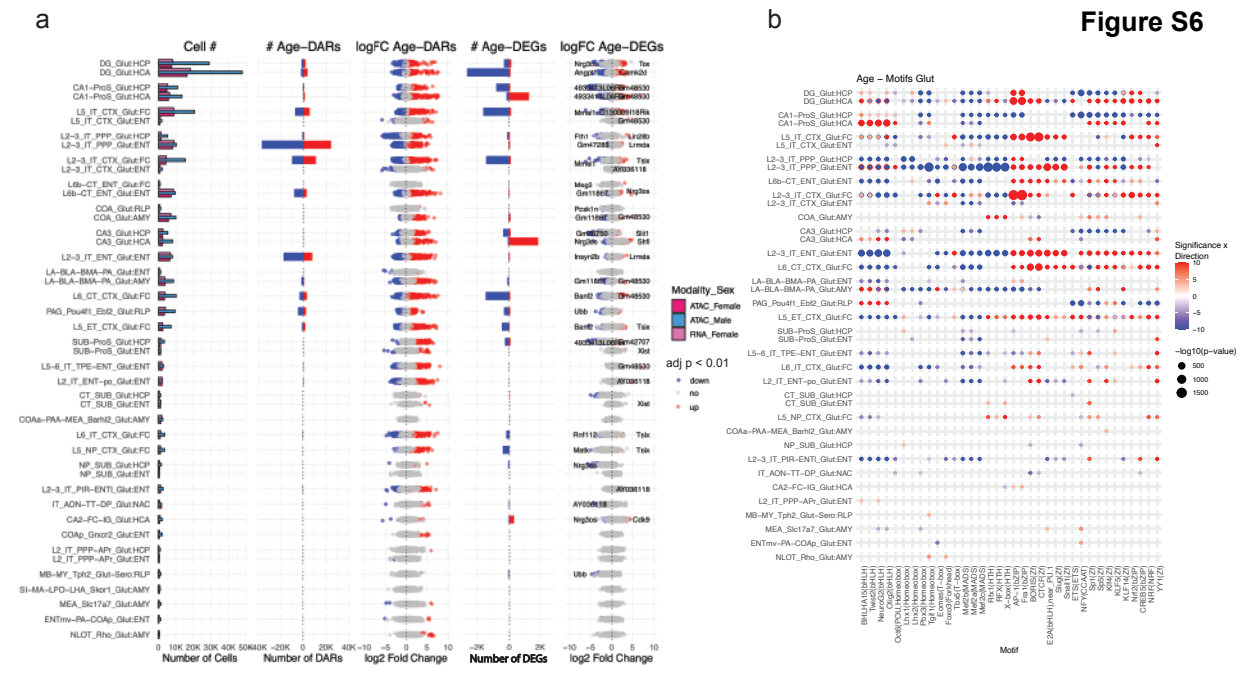
a
Cell #
Age–DARs
logFC Age–DARs
Age–DEGs
logFC Age–DEGs
Number of Cells
Number of DARs
log2 Fold Change
Number of DEGs
log2 Fold Change
Modality_Sex
ATAC_Female
ATAC_Male
RNA_Female
adj p < 0.01
down
no
up
b
Age – Motifs Glut
Motif
Significance x Direction
−log10(p−value)
500
1000
1500

a

MERFISH vs RNA Pearson Correlation

Figure S7

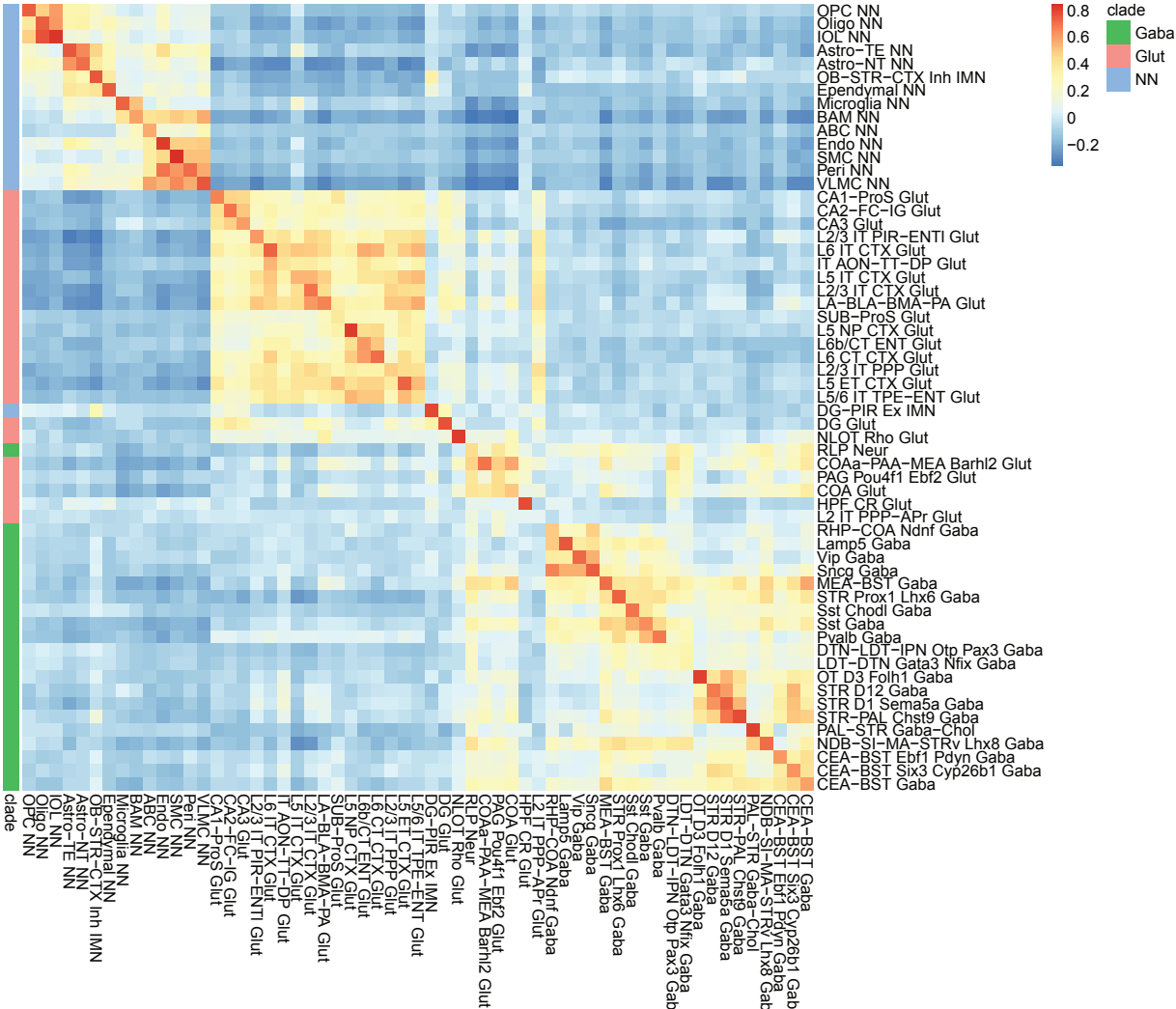

Figure S8

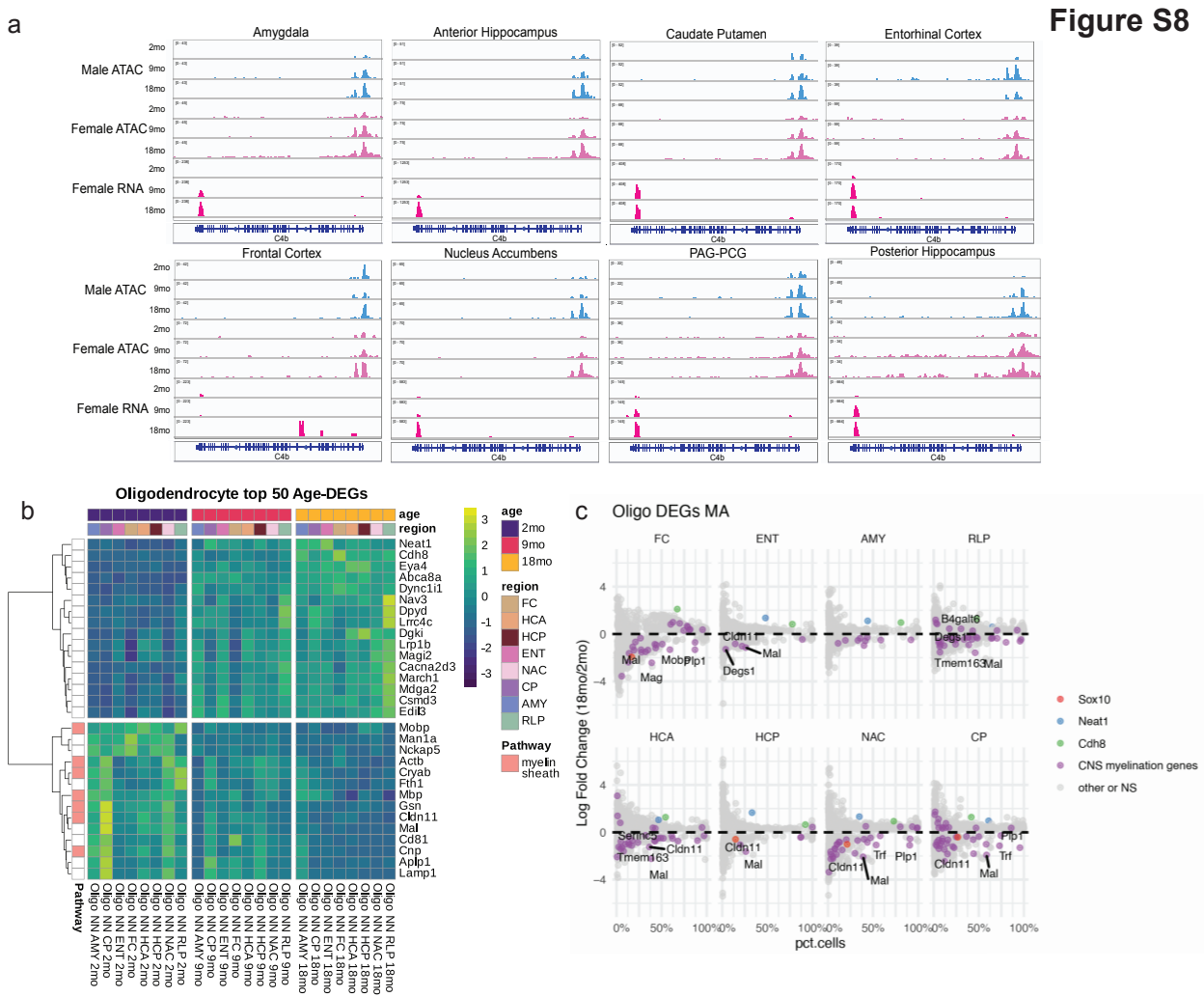
a
Amygdala
Anterior Hippocampus
Caudate Putamen
Entorhinal Cortex
Frontal Cortex
Nucleus Accumbens
PAG-PCG
Posterior Hippocampus
Male ATAC
Female ATAC
Female RNA
2mo
9mo
18mo
C4b
b
Oligodendrocyte top 50 Age-DEGs
age
region
Neat1
Cdh8
Eya4
Abca8a
Dync1i1
Nav3
Dpyd
Lrfc4c
Dgki
Lrp1b
Magi2
Cacna2d3
March1
Mdga2
Csmd3
Edil3
Mobp
Man1a
Nckap5
Actb
Cryab
Fth1
Mbp
Gsn
Cldn11
Mal
Cd81
Cnp
Aplp1
Lamp1
2mo
9mo
18mo
FC
HCA
HCP
ENT
NAC
CP
AMY
RLP
Pathway
myelin sheath
Oligo NN RLP 2mo
Oligo NN NAC 2mo
Oligo NN HCP 2mo
Oligo NN HCA 2mo
Oligo NN FC 2mo
Oligo NN ENT 2mo
Oligo NN AMY 2mo
Oligo NN CP 9mo
Oligo NN AMY 9mo
Oligo NN ENT 9mo
Oligo NN FC 9mo
Oligo NN HCA 9mo
Oligo NN HCP 9mo
Oligo NN NAC 9mo
Oligo NN RLP 9mo
Oligo NN AMY 18mo
Oligo NN CP 18mo
Oligo NN ENT 18mo
Oligo NN FC 18mo
Oligo NN HCA 18mo
Oligo NN HCP 18mo
Oligo NN NAC 18mo
Oligo NN RLP 18mo
c
Oligo DEGs MA
FC
ENT
AMY
RLP
HCA
HCP
NAC
CP
Log Fold Change (18mo/2mo)
pct.cells
Sox10
Neat1
Cdh8
CNS myelination genes
other or NS

Figure S9

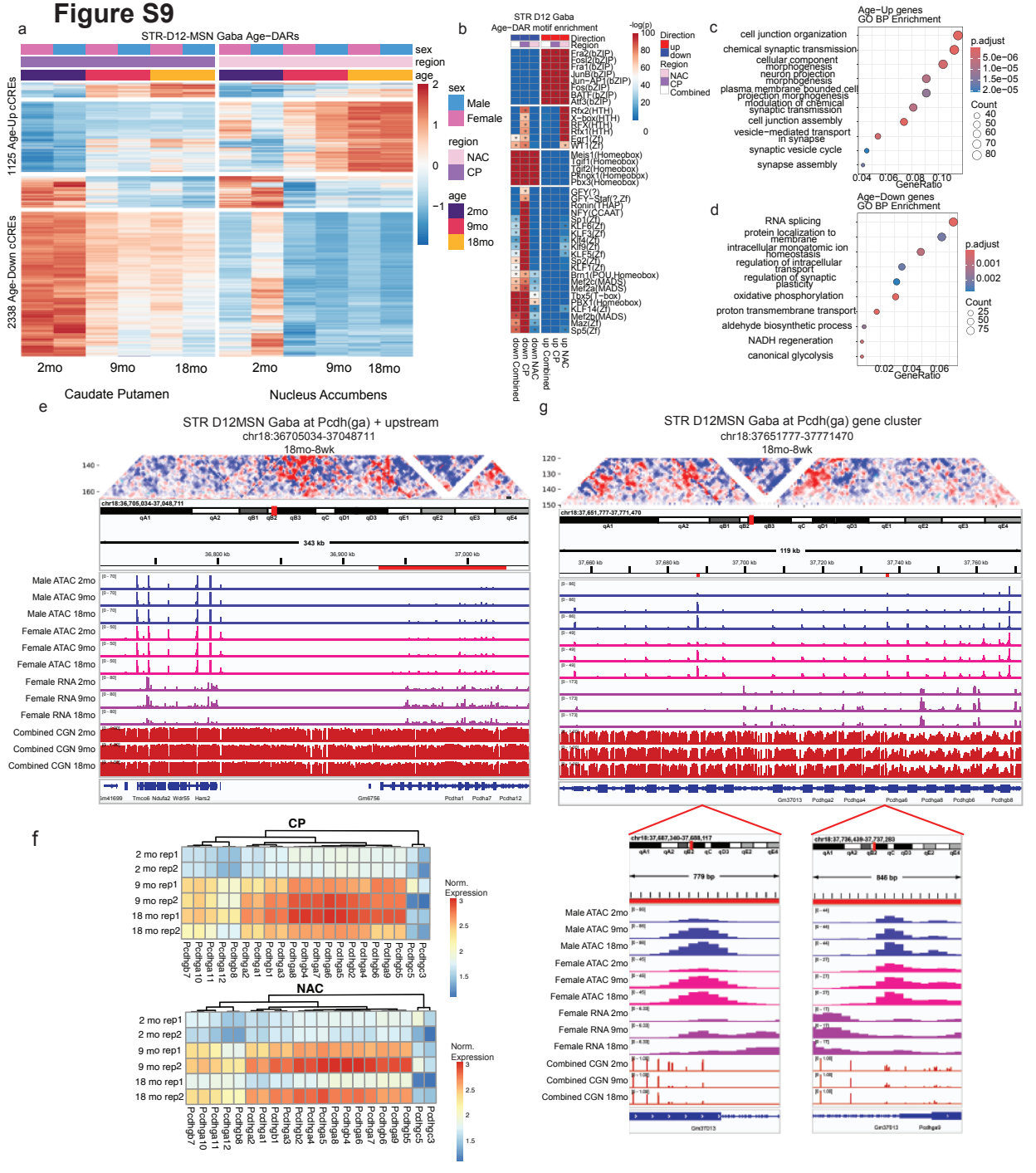
a
STR-D12-MSN Gaba Age−DARs
sex
region
age
1125 Age-Up cCREs
2338 Age-Down cCREs
2mo
9mo
18mo
Caudate Putamen
Nucleus Accumbens
Male
Female
NAC
CP
2mo
9mo
18mo
b
STR D12 Gaba
Age−DAR motif enrichment
Direction
Region
up
down
NAC
CP
Combined
-log(p)
c
Age−Up genes
GO BP Enrichment
cell junction organization
chemical synaptic transmission
cellular component morphogenesis
neuron projection morphogenesis
plasma membrane bounded cell projection morphogenesis
modulation of chemical synaptic transmission
cell junction assembly
vesicle−mediated transport in synapse
synaptic vesicle cycle
synapse assembly
GeneRatio
p.adjust
Count
d
Age−Down genes
GO BP Enrichment
RNA splicing
protein localization to membrane
intracellular monoatomic ion homeostasis
regulation of intracellular transport
regulation of synaptic plasticity
oxidative phosphorylation
proton transmembrane transport
aldehyde biosynthetic process
NADH regeneration
canonical glycolysis
GeneRatio
p.adjust
Count
e
STR D12MSN Gaba at Pcdh(ga) + upstream
chr18:36705034-37048711
18mo-8wk
343 kb
Male ATAC 2mo
Male ATAC 9mo
Male ATAC 18mo
Female ATAC 2mo
Female ATAC 9mo
Female ATAC 18mo
Female RNA 2mo
Female RNA 9mo
Female RNA 18mo
Combined CGN 2mo
Combined CGN 9mo
Combined CGN 18mo
g
STR D12MSN Gaba at Pcdh(ga) gene cluster
chr18:37651777-37771470
18mo-8wk
119 kb
f
CP
NAC
2 mo rep1
2 mo rep2
9 mo rep1
9 mo rep2
18 mo rep1
18 mo rep2
Norm. Expression
779 bp
846 bp

Figure S10

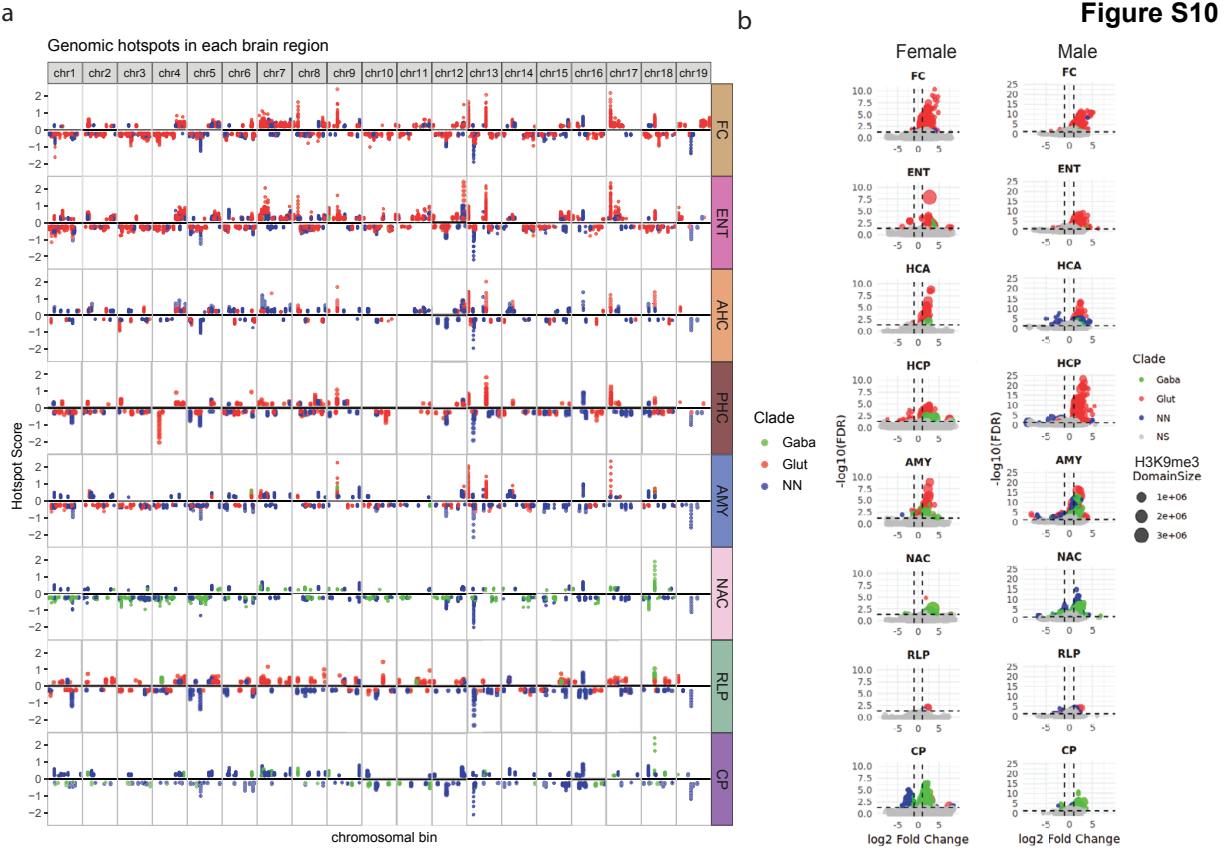
a
Genomic hotspots in each brain region
chr1
chr2
chr3
chr4
chr5
chr6
chr7
chr8
chr9
chr10
chr11
chr12
chr13
chr14
chr15
chr16
chr17
chr18
chr19
FC
ENT
AHC
PHC
AMY
NAC
RLP
CP
Hotspot Score
chromosomal bin
Clade
Gaba
Glut
NN
b
Female
Male
FC
ENT
HCA
HCP
AMY
NAC
RLP
CP
-log10(FDR)
log2 Fold Change
Clade
Gaba
Glut
NN
NS
H3K9me3
DomainSize
1e+06
2e+06
3e+06

Figure S11

a

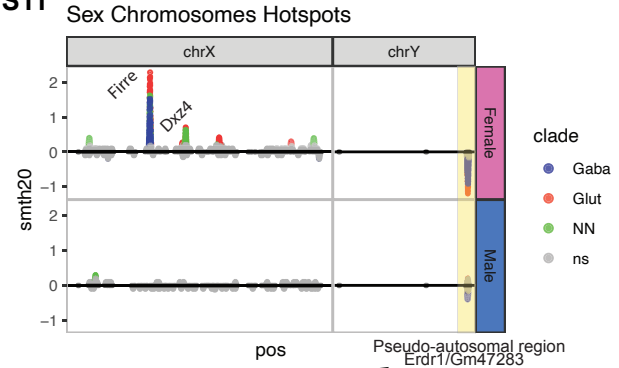

b

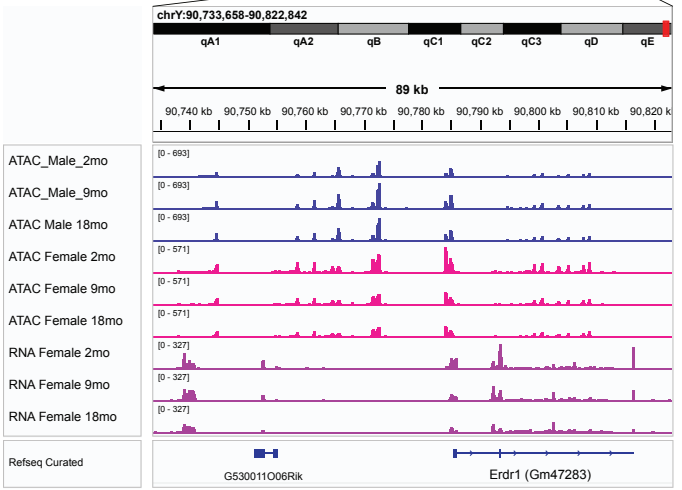

c

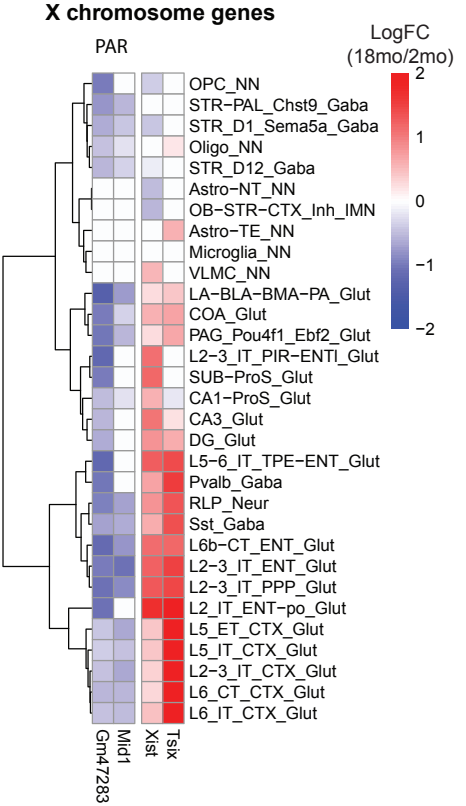

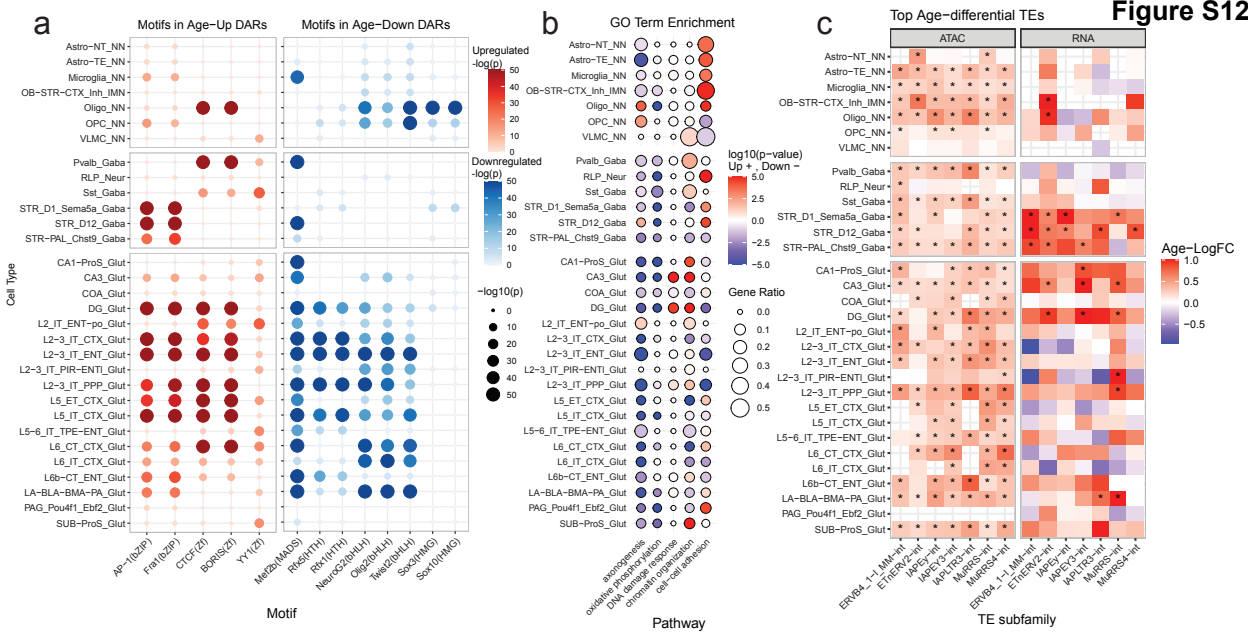
Figure S12
a
Motifs in Age−Up DARs
Motifs in Age−Down DARs
Astro−NT_NN
Astro−TE_NN
Microglia_NN
OB−STR−CTX_Inh_IMN
Oligo_NN
OPC_NN
VLMC_NN
Pvalb_Gaba
RLP_Neur
Sst_Gaba
STR_D1_Sema5a_Gaba
STR_D12_Gaba
STR−PAL_Chst9_Gaba
CA1−ProS_Glut
CA3_Glut
COA_Glut
DG_Glut
L2_IT_ENT−po_Glut
L2−3_IT_CTX_Glut
L2−3_IT_ENT_Glut
L2−3_IT_PIR−ENTI_Glut
L2−3_IT_PPP_Glut
L5_ET_CTX_Glut
L5_IT_CTX_Glut
L5−6_IT_TPE−ENT_Glut
L6_CT_CTX_Glut
L6_IT_CTX_Glut
L6b−CT_ENT_Glut
LA−BLA−BMA−PA_Glut
PAG_Pou4f1_Ebf2_Glut
SUB−ProS_Glut
Cell Type
AP−1(bZIP)
Fra1(bZIP)
CTCF(Zf)
BORIS(Zf)
YY1(Zf)
Mef2b(MADS)
Rfx5(HTH)
Rfx1(HTH)
Neurod2(bHLH)
Olig2(bHLH)
Twist2(bHLH)
Sox3(HMG)
Sox10(HMG)
Motif
Upregulated
-log(p)
Downregulated
-log(p)
−log10(p)
b
GO Term Enrichment
axonogenesis
oxidative phosphorylation
DNA damage response
chromatin organization
cell−cell adhesion
Pathway
log10(p−value)
Up + _Down −
Gene Ratio
c
Top Age−differential TEs
ATAC
RNA
ERVB4_1−I_MM−int
ETnERV2−int
IAPEz−int
IAPEY3−int
IAPLTR3−int
MuRRS−int
MuRRS4−int
TE subfamily
Age−LogFC

Figure S13

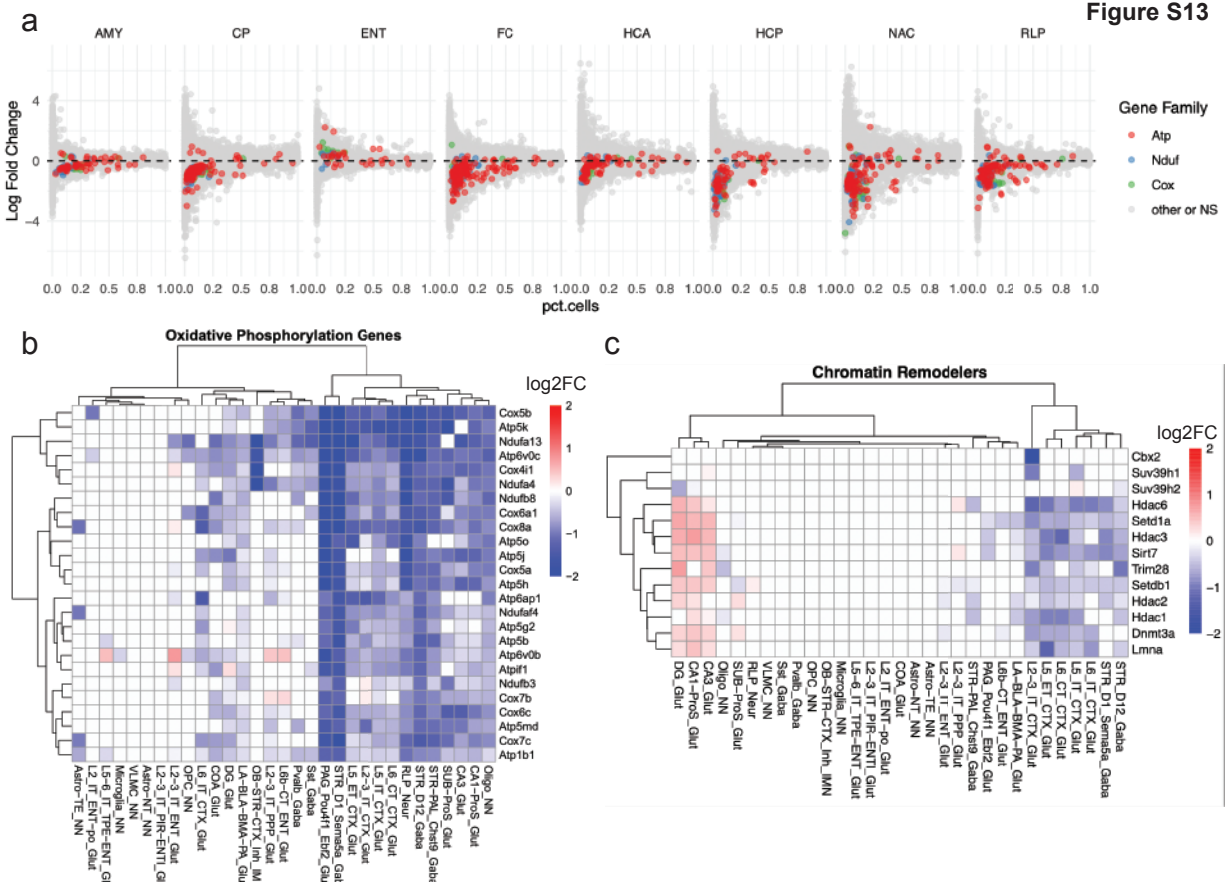
a
AMY
CP
ENT
FC
HCA
HCP
NAC
RLP
Log Fold Change
pct.cells
Gene Family
Atp
Nduf
Cox
other or NS
b
Oxidative Phosphorylation Genes
log2FC
Cox5b
Atp5k
Ndufa13
Atp6v0c
Cox4i1
Ndufa4
Ndufb8
Cox6a1
Cox8a
Atp5o
Atp5j
Cox5a
Atp5h
Atp6ap1
Ndufaf4
Atp5g2
Atp5b
Atp6v0b
Atpif1
Ndufb3
Cox7b
Cox6c
Atp5md
Cox7c
Atp1b1
c
Chromatin Remodelers
log2FC
Cbx2
Suv39h1
Suv39h2
Hdac6
Setd1a
Hdac3
Sirt7
Trim28
Setdb1
Hdac2
Hdac1
Dnmt3a
Lmna